buildings

MDPI

Article

Steel Moment Frames with Reduced Web Section Connections: Bilin Parameters and Application of Machine Learning

Ali Karami [1,2], Konstantinos Daniel Tsavdaridis [1,3], Fahad Falah Almutairi [4] and Andrés Alonso-Rodriguez [5,*]

[1] Department of Engineering, School of Science & Technology, City St George's, University of London, Northampton Square, London EC1V 0HB, UK; itisalikarami@gmail.com (A.K.); konstantinos.tsavdaridis@city.ac.uk (K.D.T.)
[2] Department of Civil and Environmental Engineering, Faculty of Engineering, University of Auckland, Private Bag 92019, Auckland 1142, New Zealand
[3] Institute of Seel Structures, School of Civil Engineering, National Technical University of Athens, 9, Zografou Campus, Iroon Polytechneiou Str., GR-15780 Athens, Greece
[4] Department of Civil & Architectural Engineering, College of Engineering, International University of Science and Technology in Kuwait, Al-Ardiya 92400, Kuwait; fahad.almutairi@ku.edu.kw
[5] Department of Civil, Environmental and Architectural Engineering, University of Padova, Via Marzolo 9, 35131 Padova, Italy
* Correspondence: andalon@gmail.com

Abstract

This paper investigates the seismic performance of reduced web section (RWS) connections in steel moment frames. Such an outcome is reached by employing advanced machine learning and deep learning techniques to predict the modified Ibarra–Medina–Krawinkler (IMK) Bilin parameters for RWS connections across various configurations. A database of 154 specimens from experimental and finite element studies was analysed, focusing on non-composite RWS connections. The study develops and compares multiple predictive models, including Random Forest, Neural Networks, Support Vector Regression, Gradient Boosting, XGBoost, and deep learning, to predict IMK Bilin parameters with high accuracy. It was found that XGBoost consistently demonstrated superior performance across all assessed metrics, having error metrics (MSE, MAE, Pearson and Spearman correlations, MAPE, and ROC area under the curve) at least an order of magnitude below its counterparts or significantly outperforming. Feature importance analysis revealed complex interactions between geometric properties and connection behaviour, with web slenderness and span-to-depth ratio playing critical roles. Additionally, pushover analyses were conducted on 2-, 4-, 8-, 12-, and 20-story benchmark frames to associate the global seismic behaviour of frames with RWS and RBS connections. Results indicate that RWS connections often provide higher strength and comparable or superior ductility to their counterparts, especially in low to mid-rise structures. All RWS configurations achieved interstorey drifts exceeding 4%, meeting ANSI/AISC and EC8 performance targets. Hence, the work showcased contributes to the adoption of RWS connections for retrofitting purposes by providing a robust tool for structural engineers to incorporate RWS connections into performance-based seismic design.

Keywords: reduced web section; steel moment frames; seismic performance; machine learning; Ibarra–Medina–Krawinkler model

Check for updates

Academic Editor: Eric M. Lui

Received: 23 August 2026
Revised: 6 October 2026
Accepted: 15 October 2026
Published: 26 October 2026

Copyright: © 2026 by the authors. Licensee MDPI, Basel, Switzerland. This article is an open access article distributed under the terms and conditions of the Creative Commons Attribution (CC BY) license.

1. Introduction

The design of steel moment-resisting frames (MRFs) has evolved significantly, driven by lessons from major seismic events, notably the 1994 Northridge and 1995 Kobe earthquakes. These events exposed critical vulnerabilities in beam-to-column connections, particularly in welded flange-bolted web details, where brittle failures occurred due to rapid crack propagation from the beam flange into the column at joints [1–3]. These failures prompted a shift toward performance-based design methodologies, placing emphasis on enhanced ductility, energy dissipation, and overall seismic performance in steel MRFs.

This led to the development of the SAC initiative, which aimed at developing prequalified connections that ensure the development of plastic hinges at designated locations, i.e., protected zones. Thus, fragile failure is precluded, as only ductile yield modes are allowed [4,5]. Subsequent advancements introduced other approaches, amongst them reduced web section (RWS) connections. They optimise steel usage and facilitate utility installation through perforations on the beam's web. Yet they showcase ductile behaviour when subjected to cyclic action [3–9].

Ductile behaviour of RWS connections has been verified through laboratory testing, although full prequalification hasn't been achieved to the best of the authors' knowledge. Results indicate that RWS connections, can reach interstorey drift demands of 4%, meeting performance targets set by American National Standards Institute/American Institute of Steel Construction (ANSI/AISC) and Eurocode 8 (EC8) standards [10–20] for inclusion in Special Moment Frames SMFs. Moreover, Erfani et al. proposed a design procedure for sizing web openings in RWS beams, showing through nonlinear static analysis that these connections reduce building elastic stiffness by 2.5–8.5% and ultimate base shear by 3.5–6%, while clustering plastic behaviour around the openings. Thus, adhering to the 'strong column-weak beam' principle [21]. Similarly, Roudsari and Zangeneh demonstrated that diagonal web stiffeners in IPE reduced beam sections enhance energy dissipation and plastic rotation capacity, mitigating issues like web local buckling and lateral torsional buckling [22].

Beyond connection-level improvements, complementary strategies for enhancing the seismic performance of steel-framed buildings have been investigated at the global system level, including the coupling of adjacent planar steel frames by rigid bars to control inter-storey drifts and accelerations under strong ground motions [23].

Henceforth, there is interest in advancing understanding of behaviour at micro-scale and testing of connections into macro modelling to investigate building behaviour with RWS connections to strong ground shaking. One of the most versatile models for representing connection behaviour at meso-scale (rotation-moment hysteresis rules) is the modified Ibarra–Medina–Krawinkler (IMK) model [5]. Thus, this study aims at predicting the parameters of the IMK model for RWS connections, considering their geometry.

Consequently, this research undertakes a thorough analysis of a recently compiled database encompassing all publicly available experimental and finite element (FE) studies of RWS connections [21]. Main outcomes are hysteresis plots of connections with diverse geometries, and structural configurations. Afterwards, experimental settings are replicated in Opensees [5] using beam elements, connected to springs that follow the IMK hysteresis. Then Artificial Intelligence (AI) is employed to adjust parameters for each experiment to formulate predictive algorithms for estimating IMK model parameters based on the geometry of RWS connections, focusing on web slenderness, span-to-depth ratios and perforation size and location from the column face. Thereby, the effects of RWS connections on building behaviour will be explored by effectuating push-over analyses for different study cases (2 stories, 4 stories, 8 stories, 12 stories, and 20 stories).

Although machine learning has already been used to predict IMK parameters of steel members and connections [24–26], but, to the best of the authors' knowledge, not for connections with a perforated beam web. The contributions of this study are: (i) a set of modified-IMK (Bilin) parameters for 154 non-composite RWS connections, obtained by fitting the complete cyclic moment–rotation response of each specimen, with separate parameters for positive and negative bending; (ii) data-driven models that predict the parameters that vary across the database from six dimensionless inputs, two of which describe the opening o/hb and So/hb), with six algorithms compared under the same data split and the same cross-validation; (iii) an openly accessible tool that returns a complete Bilin input set for OpenSees or commercial software; and (iv) pushover analyses of frames from 2 to 20stories in which, unlike earlier pushover studies of RWS frames [6], the RWS hinges follow cyclic-deterioration parameters calibrated on test and FE data. The database is smaller than that of Horton et al. [24]; the contribution of this work is the extension of the approach to perforated-web connections, not a larger dataset.

The outcomes of this research to offer structural engineers practical tools and evidence-based recommendations for incorporating RWS connections into performance-based seismic design frameworks, particularly by estimating bounds on systemic static overstrength and enhanced flexibility. In detail, it provides a way to incorporate findings of complex high-fidelity finite element models into commercial structural engineering software, thus allowing practitioners a streamlined way to employ RWS connections in the seismic design of buildings. Hence contributing to improving the seismic resilience of steel structures.

2. Recent Development in Modelling and Analysis of Steel Moment Connections

2.1. Advancements in Modelling Techniques

The modified Ibarra–Medina–Krawinkler (IMK) model has become a cornerstone in FE modelling of steel moment connections. This phenomenological model represents the moment-rotation behaviour through a trilinear backbone curve with cyclic deterioration rules [22].

IMK Model Formulation:

The model backbone curve (Figure 1) is characterised by several key parameters including the initial elastic stiffness (K_0 = 6EI/L for fixed-end beams), the effective yield moment (M_y) and plastic moment (M_c), the pre-capping plastic rotation (θ_p) and post-capping rotation capacity (θ_{pc}), and the residual strength ratio (M_r/M_c). The cyclic deterioration is governed by an energy-based parameter where E_i is the hysteretic energy dissipated, E_t is the total energy dissipation capacity, and c is the deterioration rate exponent.

$$\beta = \left(\frac{E_i}{E_t \cdot M_y \cdot \theta_p}\right)^c \quad (1)$$

This model was modified specifically for steel beams with Reduced Beam Section (RBS) by Lignos and Krawinkler [22,27], incorporating empirical relationships for the backbone parameters as functions of geometric and material properties [27]. The modified IMK model captures multiple deterioration modes including basic strength deterioration, which represents the reduction in peak moment capacity, post-capping strength deterioration characterised by accelerated strength loss after the peak moment is reached, unloading stiffness deterioration reflecting the reduction in elastic stiffness during unloading cycles, and accelerated reloading stiffness deterioration manifested as pinching behaviour in the hysteresis loops.

These features allowed for more accurate simulations of the complex hysteretic behaviour observed in steel moment connections under cyclic loading, particularly capturing strength and stiffness degradation observed in experimental tests [22,28].

Calibration of IMK parameters:

The original calibration of the modified Ibarra–Medina–Krawinkler (IMK) model was conducted by Lignos and Krawinkler [29] based on a database of more than 300 cyclic tests on standard wide-flange steel beams and Reduced Beam Section (RBS) connections. From this database, empirical predictive equations were proposed for the pre-capping plastic rotation θ_p, the post-capping plastic rotation θ_{pc} and the reference cumulative-energy parameter Λ, as functions of cross-section geometry, shear-span ratio and material properties. These equations remain the most widely adopted reference values for IMK calibration of steel wide-flange members.

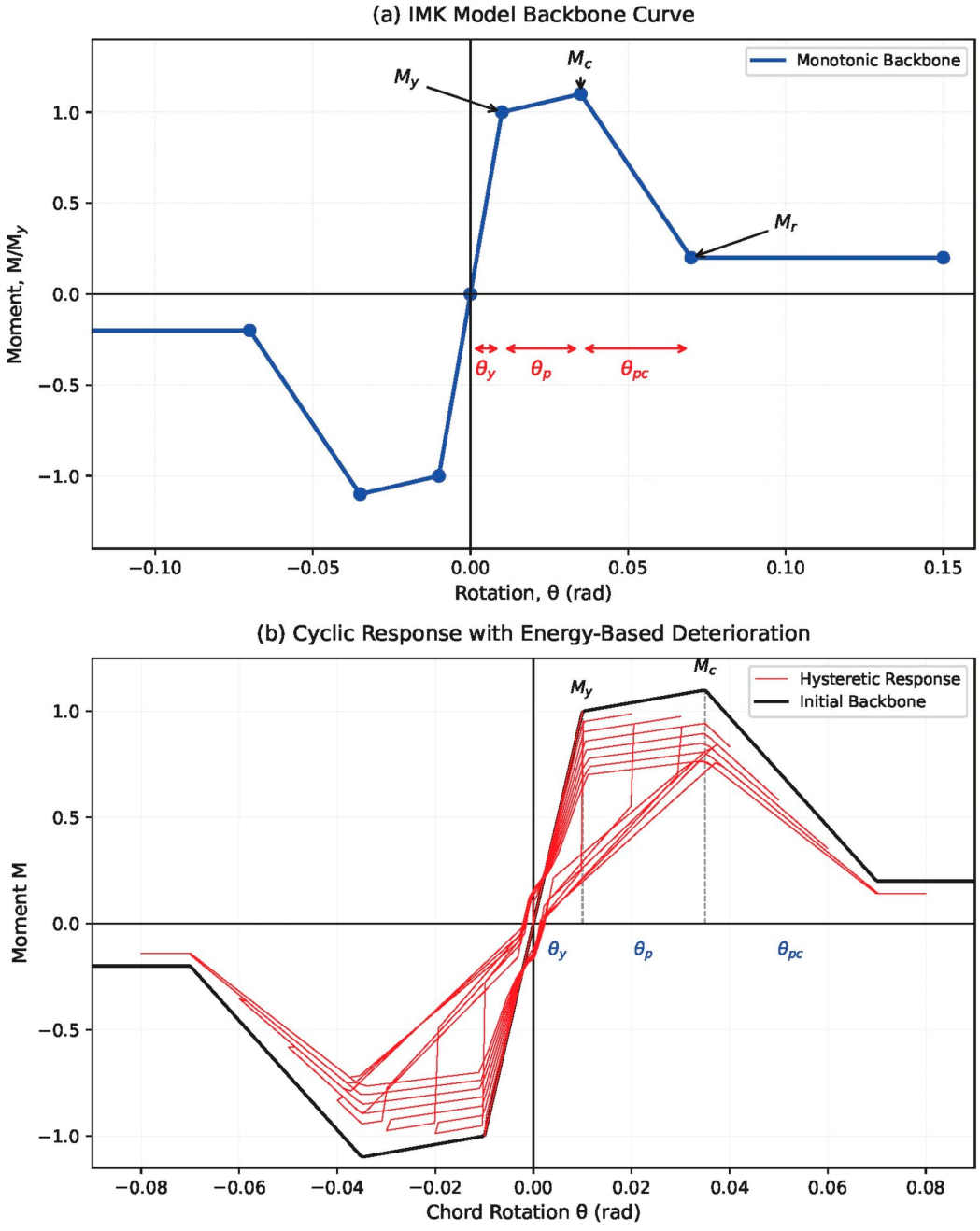


Figure 1. Schematic representation of IMK model backbone curve and hysteretic response.

In the years following the original work, dedicated calibration campaigns have extended the IMK model to a number of structural systems not covered by the Lignos and Krawinkler database. Bosco et al. [30] derived a new set of predictive equations for cold-formed hollow steel sections used as columns in moment-resisting frames, calibrating the model against detailed finite element simulations. Bamshad et al. [31] applied the modified Ibarra-Krawinkler formulation to one-storey steel plate shear walls, while Qi et al. [32] combined a monotonic curve with the IMK hysteretic model to capture the deterioration of H-shaped beams induced by local buckling of the flange and web plates. Şahin et al. [33] extended the model to composite steel-concrete beams, reporting approximately 20% greater cyclic degradation than in bare steel counterparts. Moammer et al. [34] developed predictive equations for shear links in eccentrically braced frames, while applications to concrete-filled steel tubes [35] and to reinforced concrete columns [36,37] have also been reported. In all of these studies, the calibration follows broadly the same procedure: a numerical or experimentally sourced hysteresis response is replicated through curve-fitting following hysteresis rules. The parameters governing the latter are found after performing analyses or machine learning.

2.2. Integration of Machine Learning

More recent studies have moved from closed-form predictive equations to machine learning approaches that infer parameters of the of IMK model. Horton et al. [24] developed a deep-learning framework predicting seven IMK parameters for RBS connections from beam and RBS geometry, trained on a database of 1480 finite-element models validated against experiments and released as a MATLAB (2019 ver.) toolbox; the reported accuracy reached from 96 to 98% across the seven parameters. Khoshkroodi et al. [25] proposed a stacking ensemble of AdaBoost, Random Forest, and XGBoost to predict the pre-capping plastic rotation, the post-capping plastic rotation, and the cumulative rotation capacity Λ for steel W-section beams, with the web-depth-over-web-thickness ratio h/t_w and the flange slenderness ratio $b_f/2t_f$ emerging as the dominant predictors through SHAP analysis. Chen et al. [36] applied a Random Forest model combined with active learning to predict seven IMK parameters for 475 reinforced concrete columns, while Tasdemir et al. [26] developed an explainable ML framework using ANN, Random Forest, SVM, Gradient Boosting and Ridge Regression for the prediction of moment-rotation backbone curves of RBS connections, with the ANN achieving an R^2 of 0.9996. Shayanfar et al. [35] used artificial neural networks to predict the parameters of a deterioration model for compact square concrete-filled steel tube columns.

3. Methodology

3.1. Data Collection and Analysis

This study builds upon a database of test results of RWS connections compiled by Almutairi and Tsavdaridis [28]. Machine learning (ML) and deep learning (DL) models are applied to the raw data to estimate the IMK bilin parameters for various RWS connection configurations. The RWS database [28] curated data from 14 experimental and finite element studies, comprising a comprehensive dataset of 251 specimens and 247 FE models of RWS connections, including both bare steel and composite configurations, alongside 14 solid webbed-beam connections used as benchmarks.

For the present study, the model considers the beam-to-column connection behaviour under the assumption of infinitely stiff columns, which effectively represents the cruciform test configuration with rigid column boundary conditions. This idealisation is consistent with the objective of isolating the connection rotational response and capturing the moment-rotation characteristics at the beam-column interface. The dataset utilised includes 154 test

specimens (as shown in Table 1) encompassing various connection types, including welded and bolted extended end-plate connections, with different geometric and material properties. Nevertheless, all had a fixed boundary condition and just replicated a single beam span. This approach ensures consistency in boundary conditions and moment-rotation behaviour, which is critical for accurate calibration of the IMK deterioration parameters.

Table 1. Non-composite RWS database from the literature.

Reference	Study	Connection	Number of Sections	Total Number of Considered Tests
Tsavdaridis et al. [11]	FE	Welded	1	3
Tsavdaridis and Papadopoulos [7]	FE	BEEP-3-R	1	1
Zhang et al. [12]	Experiment	Welded	1	1
Boushehri et al. [13]	FE	Welded	4	48
Nazaralizadeh et al. [14]	FE	BEEP-4-R	1	1
Xu et al. [15]	Experiment	Welded	1	5
Almutairi and Tsavdaridis [28]	FE	BEEP-4-R	1	95
Total Number of FE/Experimental tests				154

Likewise, the following parameters have been identified as the most critical in defining the response of a RWS connection to cyclic actions: the total height of the section h_b, the thickness of the web t_w, the flange width b_f, and the thickness of the flange t_f, as shown in Figure 2. The yield strength is denoted as f_{yb}, while L_b represents the length of the beam. Additionally, d_o indicates the diameter of the web opening and S_o indicates the distance from the web opening centreline to the edge of the column.

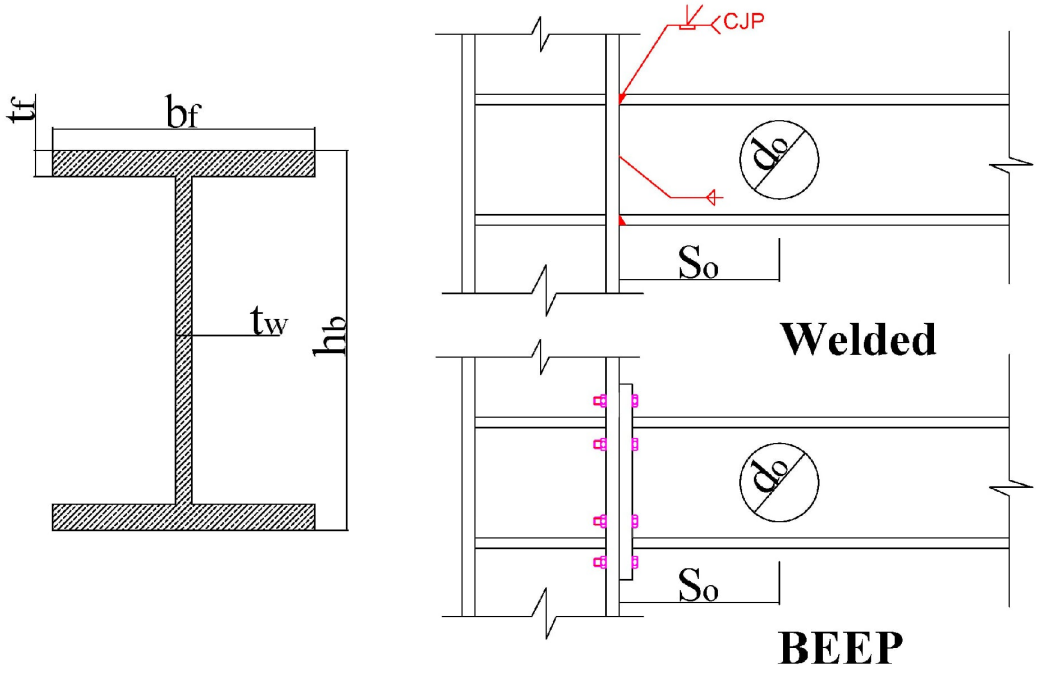


Figure 2. RWS connection parameters.

3.1.1. Modelling Approach

The benchmarking model considered in this study represents half of a cruciform test configuration, with an infinitely strong and stiff column (Figure 3). This idealisation assumes that the inflexion point occurs at the beam midspan, consistent with the theoretical framework upon which the IMK model formulation is based [10]. By modelling the connection as a cruciform subassembly with rigid column boundary conditions, the rotational behaviour of the beam-to-column connection is isolated, allowing for detailed sensitivity analyses on the RWS perforation geometry and its influence on the connection performance. This choice represents the greatest share of experimental setups and FEM models available, as beam stubs are joined to reaction walls or extremely stiff and short columns. Thereby, the focus is on the beam behaviour while considering a zero rotation at the joint (close to zero rotation at the column end). To the best of the knowledge of the authors, there is not even a single test for full cruciform setups involving RWS connections.

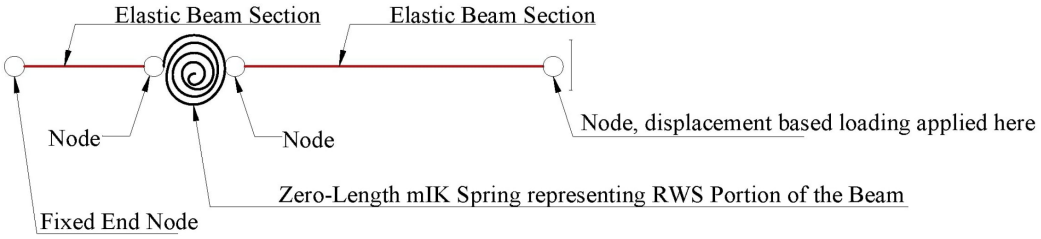


Figure 3. The equivalent zero-length spring model in OpenSees simulating FE and experimental tests of database.

Moreover, this simplified half-beam representation enables efficient parametric studies while maintaining consistency with the fundamental assumptions of the IMK deterioration model. Design procedures ensuring that inelastic action is constrained within the beam can be performed subsequently by computing overstrength factors based on the outcomes of this idealised subassembly. Column and panel zone flexibility can be incorporated by assembling additional rotational springs in series that represent these components, following the approach proposed by Gupta and Krawinkler [10]. This modular assemblage approach allows the calibrated connection models to be incorporated into large-scale finite element models for assessment of building behaviour under strong ground motion.

3.1.2. Loading Conditions

Cyclic displacement demands at the beam inflexion point were applied, following AISC's protocol for prequalification. Maximum interstorey drift demands reached 6% for most cases, while some were taken up to 5%.

3.1.3. Calibration of the Parameters Defining RWS Hysteretic Response

Least squares optimisation is employed in this study to calibrate the IMK hysteresis model parameters. This is done by replicating test results by finding the best set of parameters that lead to outcomes (i.e., hysteresis moment-chord rotation (namely, the displacement of the beam end node (away from the joint) divided by the beam length) loops from the finite element model representation) that resemble, to the closest possible extent, what was measured during experiments. The error measure to be minimised is the squared difference between them. This approach has been extensively employed in structural engineering research, particularly for the analysis of structural behaviour under seismic loads [18,19]. The proposed methodology was implemented in Python (3.12.7), using their SciPy Library. It was the tool for running OpenSees and then performing the fitting. The SciPy least-squares routine was then iterated until reaching convergence

for each specimen, with the fit accepted when the residual between the simulated and experimental moment-rotation response reached its minimum.

The parameters being optimised are:

- Cyclic deterioration parameters for strength and post-capping strength (Λ_S, Λ_C)
- Cyclic deterioration parameter for unloading stiffness (Λ_K)
- Strain-hardening ratios (a_s^+, a_s^-)
- Post-capping rotations (θ_{pc}^+, θ_{pc}^-)

3.1.4. Analysis and Post-Processing

The OpenSees implementation in this study employs dynamic, non-inertial analyses with displacement control. The solver of the equation of motion involves an optimised Newton–Raphson algorithm that follows an energy-based convergence criterion. This is useful for ensuring solution stability and accuracy in the presence of significant non-linearities. The analysis outputs node displacements and element forces are post-processed to derive the moment-rotation hysteresis curves.

3.1.5. Results of Calibration

The analysis of the modified Ibarra–Medina–Krawinkler (IMK) Deterioration Model with bilinear hysteretic response, implemented as the Bilin material in OpenSees, reveals complex interactions between web opening characteristics, beam length, and structural behaviour. The key findings encompass the effects of web opening size, position, and beam length.

Web Opening Size Effect

For relatively small and regular web opening sizes the following observations were made, (Figure 4):

- *Stiffness Degradation*: The hysteresis loops show progressive pinching as the number of displacement demand cycles increases, along with a noticeable reduction in stiffness. This behaviour is primarily governed by Λ_K parameter, as it modifies the stiffness while unloading. As rotations exceed ± 0.04 radians, the loops flatten further, indicating significant stiffness degradation. This underscores the need for precise web opening design to mitigate excessive flexibility in seismic applications.
- *Strength Preservation*: Attainment of peak moments remains consistent through multiple displacement cycles, demonstrating that the RWS connection maintains its strength capacity with minimal degradation. Hence, the Λ_S parameter seems to play a secondary role. As the provision of small web openings effectively preserves the connection's load-resisting capacity under cyclic loading. However, larger or irregular openings may introduce stress concentrations that could compromise moment-carrying capacity, warranting further study.
- *Absence of Post-Capping Phase*: Despite the pinching effect that lowers energy dissipation efficiency, the Λ_C parameter seems to play a secondary role while conditioning the response of connections with the small web openings.

For large web opening sizes, the following observations were made, as shown in Figure 5:

- *Post-Capping Phase*: There is an appreciable decline in moment capacity after reaching peak values. Yet hysteretic response remains stable at least for interstory drift demands up to ± 0.05 radians. This hints that the Λ_C parameter plays a role in conditioning response, as it governs post-capping behaviour in the IMK model.
- *Enhanced Energy Dissipation*: The loops widen as drift demands are imposed, as expected. The large web opening facilitates extensive plastic deformation in a ductile manner, increasing the enclosed loop area and thus energy dissipation. This is con-

sistent with the seismic design philosophy of RWS connections as a tool to provide adequate ductility while fostering energy dissipation.

- *More Pronounced Deterioration*: The gradual strength declines and widened loops suggest that all three IMK cyclic deterioration parameters: (Λ_S, Λ_C, and Λ_K) play significant roles in conditioning the structural response. These findings highlight the complex behaviour of RWS connections with large web openings. There is a need to balance enhanced energy dissipation with strength reduction and stiffness deterioration to achieve acceptable seismic performance.

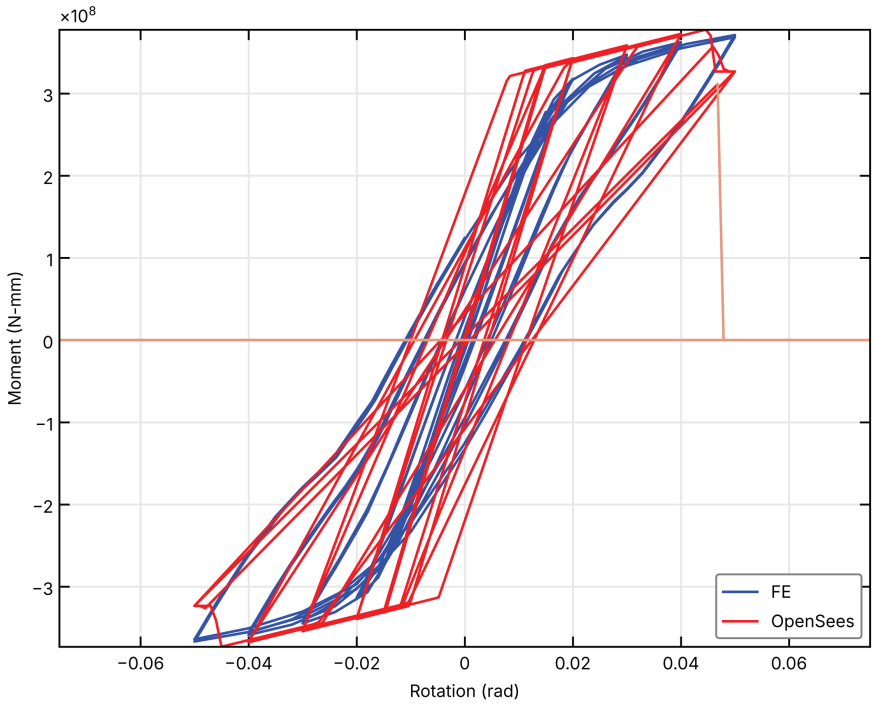


Figure 4. Calibration with the FE study [28] (web opening size): 50% of overall height of beam—distance of web opening centreline from face of column): 80% of overall height of beam.

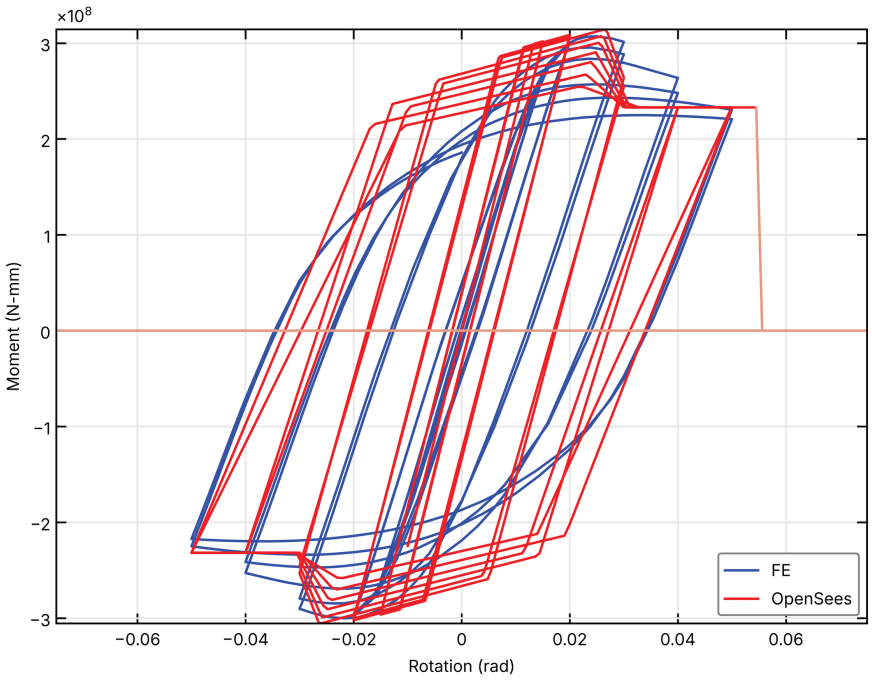


Figure 5. Calibration with the FE study [28] (web opening size): 80% of overall height of beam—(distance of web opening centreline from face of column): 80% of overall height of beam.

Web Opening Position Effect

Results indicate that the distance from the web opening centreline to the column face significantly conditions the structural behaviour of RWS connections (Figure 6):

- *StrainHardening Ratio*: It is the ratio of the post-yield (strain-hardening) stiffness to the elastic stiffness, a_s. As the distance of the centreline of the web opening from the column face increases, results indicate that the strain hardening ratio decreases.

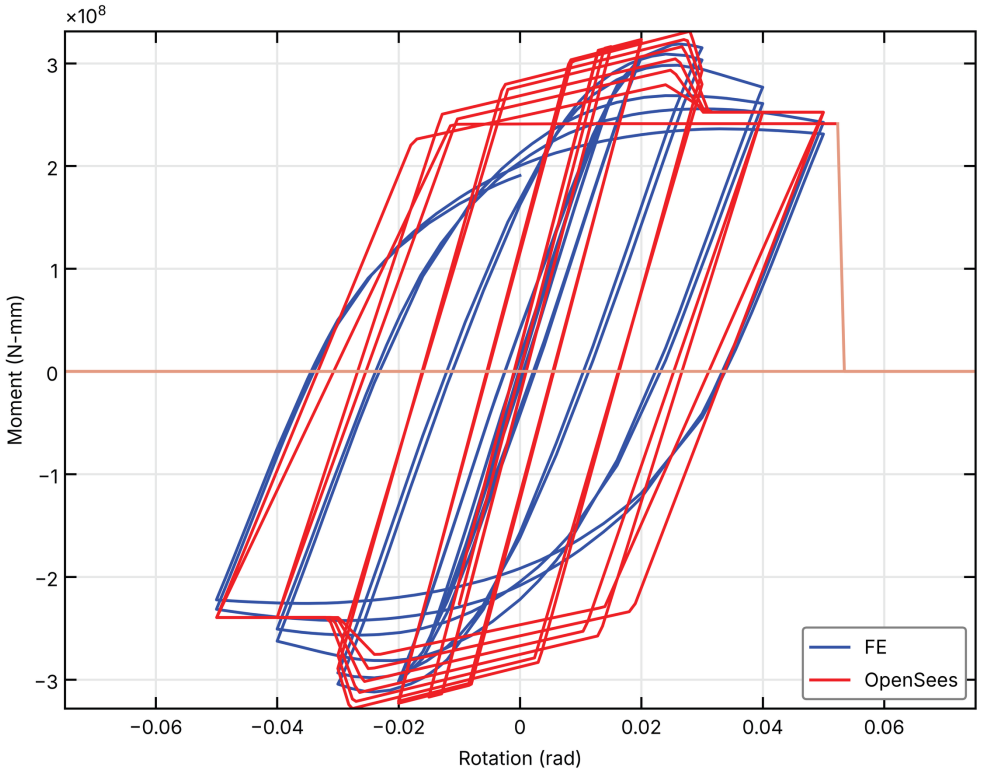


Figure 6. Calibration with the FE study [28] (web opening size): 80% of overall height of beam—(distance of web opening centreline from face of column): 105% of overall height of beam.

Thus, the web opening's position significantly influences the beam's post-yield behaviour, which in turn is a critical factor influencing seismic performance. A web opening closer to the column face (e.g., <100% of beam height) concentrates plastic strains near to the web opening, increasing the strain hardening ratio and enhancing ductility and energy dissipation capacity by clustering inelastic action there. Conversely, a more distant opening, as in the tested configuration, distributes plastic deformation across a larger beam segment, reducing localised strain hardening, increasing the chances of fragile failure modes; and eventually limiting energy absorption. This trade-off highlights the need to optimise web opening position to balance ductility, energy dissipation, and structural stability, ensuring compliance with seismic design standards such as AISC 341, which mandates a 0.04-radian drift capacity with just 20% strength loss for deployment within special moment frames. These outcomes align with findings by other researchers [1,10–12,21,38].

Effect of the Beam's Length

The beam's length has a significant impact on its structural behaviour:

- *Energy Dissipation*: As the beam length increases from 3 m to 15 m, there is a noticeable decrease in hysteretic energy dissipation. Evidently, long beams showcase smaller hysteresis loops than their shorter counterparts.
- *Rotational—Stiffness*: The increase in beam length is accompanied by a significant decrease in stiffness. The rate at which this happens is consistent with Euler–Bernoulli's theory, as stiffness is inversely proportional to the length.

- *Performance Implications*: The reduction in both energy dissipation and stiffness with increased length suggests that longer beams may experience larger deformation demands, while achieving lower hysteretic energy dissipation.

These observations highlight the complex interplay between various geometric parameters of RWS joints. Figure 7 illustrates the effect of beam length on decreasing energy dissipation and stiffness:

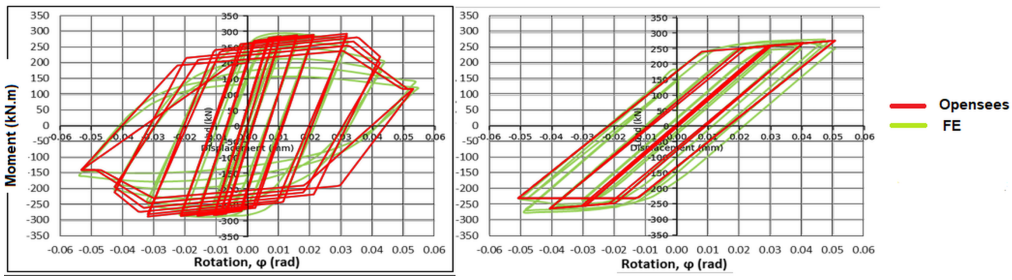


Figure 7. Effect of length of beam on decreasing energy dissipation and stiffness. Calibration with the FE study [13].

A parametric study has been conducted across all available RWS connection databases to establish quantitative relationships between geometric parameters and structural performance characteristics. The following graphs represent some results from Almutairi and Tsavdaridis [28], which demonstrate the pervasive trends observed throughout the broader database analysis.

Strain Hardening Behaviour: There is a negative correlation between the web opening's distance from the column face (S_o) and both positive and negative strain hardening ratios (a_s^+ and a_s^-), as shown in Figures 8 and 9. The positive strain hardening ratio decreases linearly from approximately 0.067 to 0.040 as S_o increases from 220 mm to 380 mm. Similarly, the negative strain hardening ratio exhibits a more pronounced decline from approximately 0.115 to 0.045 over the same distance range. This asymmetric behaviour between positive and negative loading directions indicates that there is some directional sensitivity in the connection response, which is critical for accurate seismic modelling under bidirectional loading conditions.

Unloading Stiffness Deterioration: Figure 10 presents the relationship between the web opening-to-beam height ratio (d_o/h_b) and the cyclic deterioration parameter (Λ_K). Lower Λ_K values correlate with accelerated unloading stiffness reduction per cycle, whereas higher values correspond to lower stiffness degradation during cyclic reversals. The parameter exhibits a direct positive relationship with the web opening size, increasing from approximately 0.1 to 0.7 as the d_o/h_b ratio increases from 0.50 to 0.80. This relationship indicates that larger web openings (elevated d_o/h_b ratios) have Λ_K values that reduce stiffness degradation, while smaller web openings (reduced d_o/h_b ratios) result in faster stiffness deterioration under cyclic loading.

Ductility Performance: The ductility (ratio of ultimate rotation to yield rotation) distribution analysis, presented in Figure 11, reveals that ductility capacity demonstrates a positive correlation with web opening size. The rotation ductility values range from approximately 2.774 to 3.147 across different opening configurations, with increased opening dimensions enhancing structural ductility under cyclic loading. This finding supports the design philosophy that larger web openings, while potentially reducing strength, can improve the connection's ability to undergo large plastic deformations without failure, thereby enhancing seismic performance through improved energy dissipation capacity.

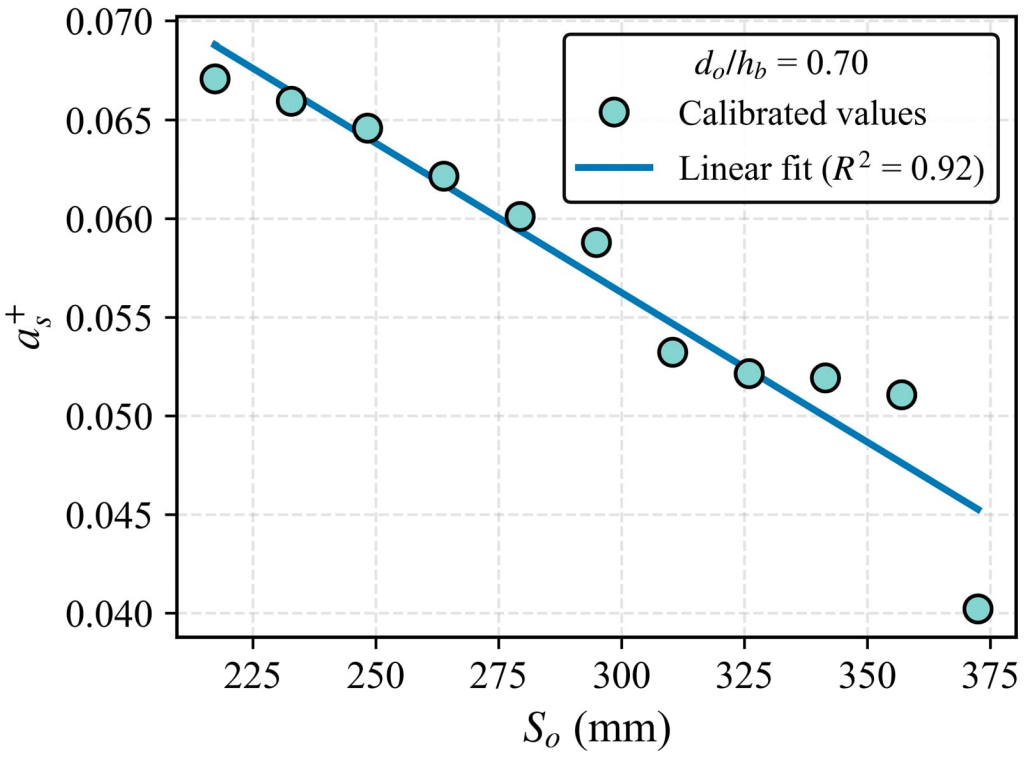


Figure 8. Variation of positive strain hardening ratio (a_s^+) with web opening centroidal distance from column face (S_o) for RWS connections with $d_o/h_b = 0.70$.

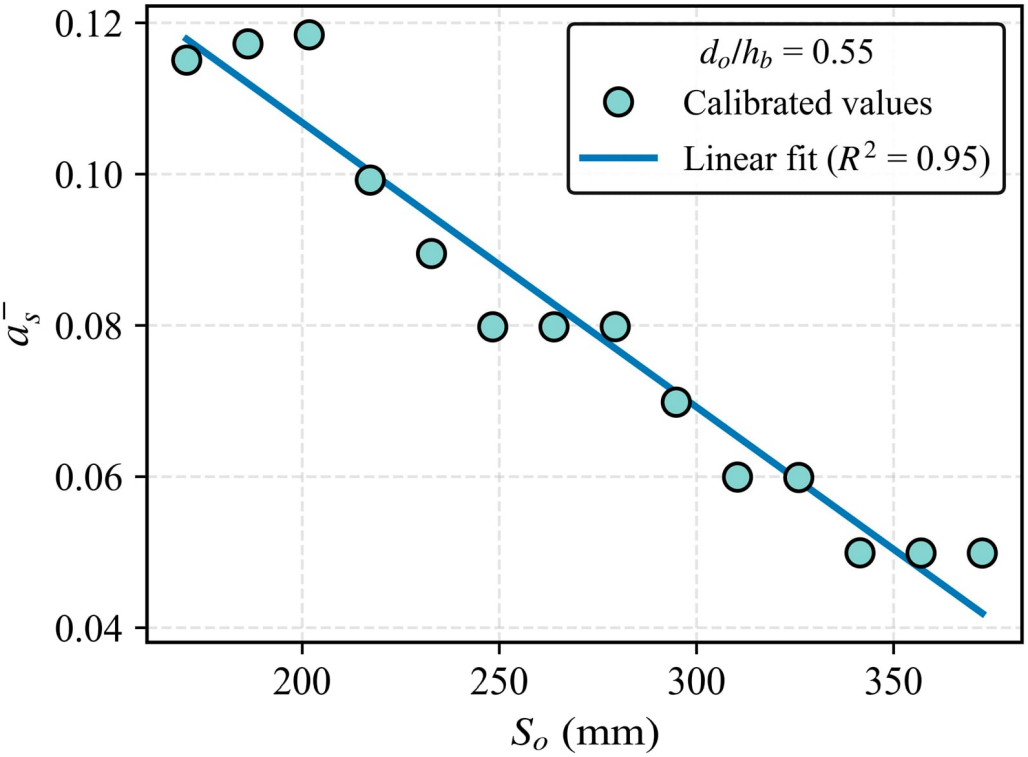


Figure 9. Variation of negative strain hardening ratio (a_s^-) with web opening centroidal distance from column face (S_o) for RWS connections with $d_o/h_b = 0.55$.

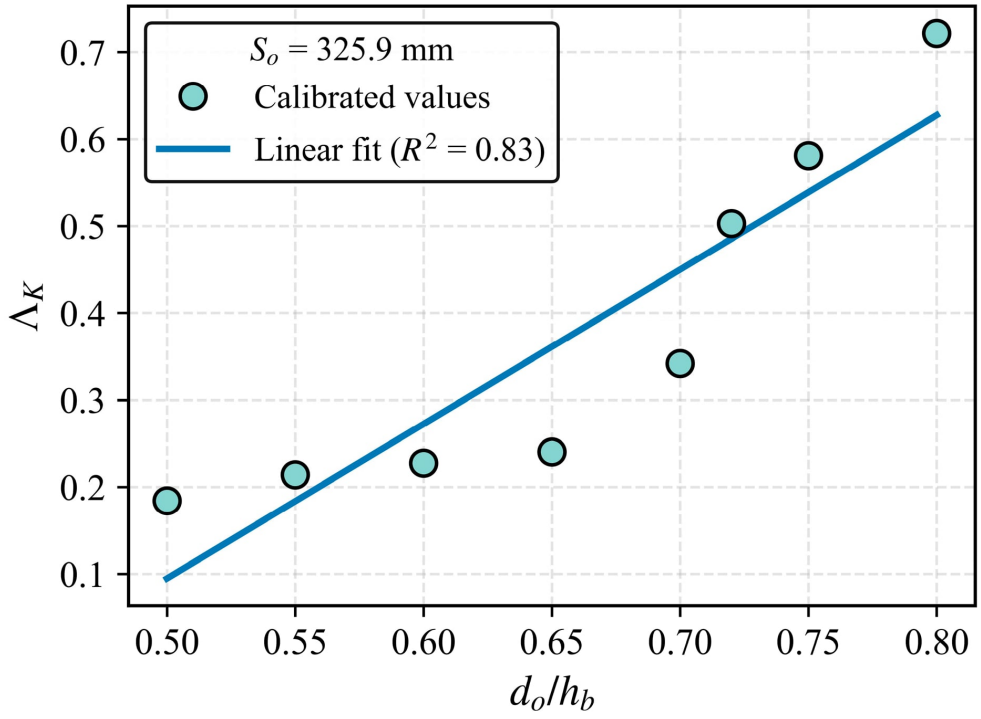


Figure 10. Variation of (Λ_K) with (d_o/h_b) for RWS connections with (S_o = 325.92 mm).

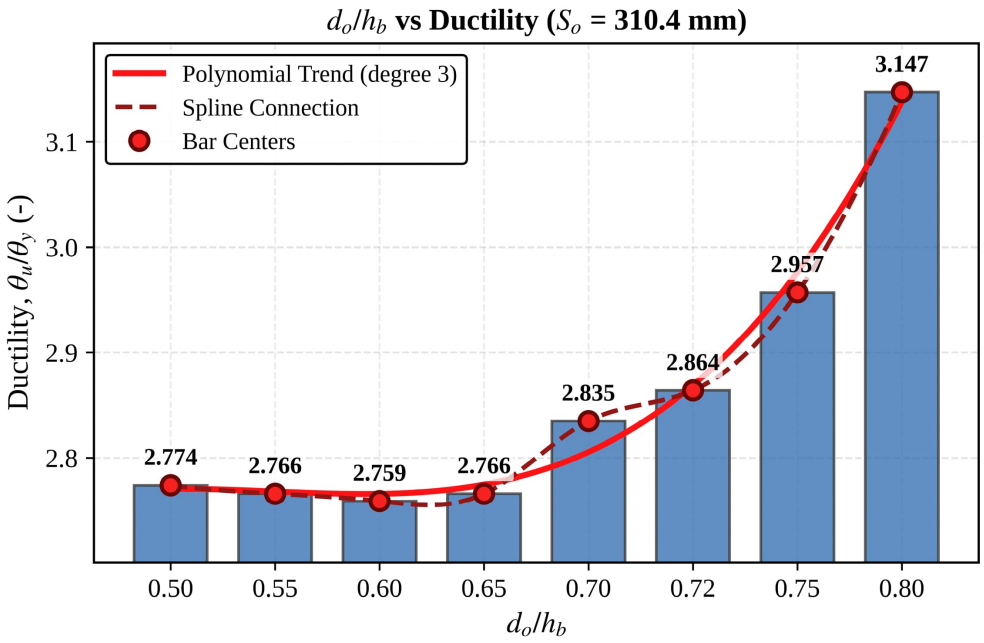


Figure 11. Variation of ductility with (d_o/h_b) for RWS connections with (S_o = 310.4 mm).

3.2. Machine Learning and Deep Learning Implementation

The large amount of data available, along with the complexity of interactions between the beam geometric parameters and trends on their hysteretic response, makes use of generalised linear models (i.e., explicit regression models) challenging. Thus, favouring AI approaches instead. Amongst them: Neural networks (NN)/Multi-Layer Perceptron (Python 3.12.7, scikit-learn 1.5.1) (MLP) regressor, random forests (RF), support vector regression (SVR), gradient boosting (GB), XGBboost (XGB), and deep learning (DL). They are available within the following Python libraries: scikit-learn, XGBoost, and TensorFlow.

3.2.1. Input Parameters

First assessment of specimens within the database, along with previous experience of the researchers, allowed them to focus on a set of parameters that play a critical role in conditioning the response of RWS connections to cyclic interstorey drift demands, namely:

- $\frac{h_b}{t_w}$: Web slenderness ratio
- $\frac{b_f}{2\times t_f}$: Flange slenderness ratio
- $\frac{L_b}{h_b}$: Beam length (shear span) to depth ratio
- $\frac{d_o}{h_b}$: Opening height ratio
- $\frac{S_o}{h_b}$: Edge distance ratio
- f_{yb}: Yield strength

Model Training and Evaluation

Figure 12 illustrates the workflow of the modelling approach employed in this study. The first data preparation involves all the preliminary work needed to take advantage of the curated database, namely, data homogenisation, error correction and normalisation. Then, diverse models are formulated and calibrated by looking at the parameters that minimise the objective function (namely, the difference between predicted and experimental hysteresis loops). This is done with an 80/20 share of the data. After training, the model undergoes Model Evaluation, which involves performance assessment by comparing how the models predict unseen outcomes. Model performance is assessed on both complexity and quantification of errors. Then, the best performing models are employed for prediction of the response. Best results are made available to end users through the provision of a graphical user interface.

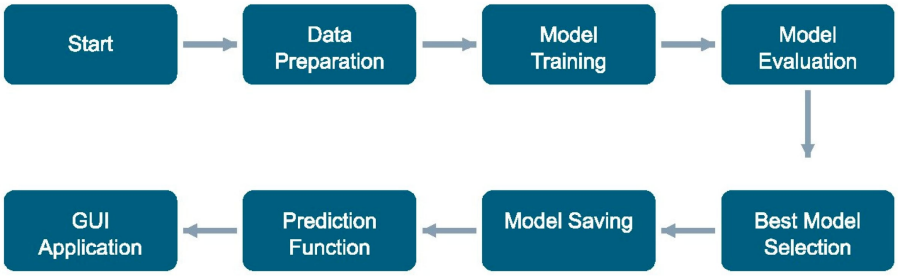


Figure 12. Python code structure overview for choosing the best prediction model.

Physical Basis

Four inputs are the dimensionless groups used in established predictive equations for steel beams and RBS connections (Lignos and Krawinkler [29]): web slenderness hb/tw, flange slenderness bf/2tf, beam length-to-depth ratio Lb/hb and yield strength fyb. They control local buckling of the web and flanges, the moment gradient along the beam and the yield strain, which govern the plastic rotation capacity and the rate of deterioration. The other two inputs are specific to RWS connections and describe the opening: its size (do/hb) and its position relative to the column face (So/hb). They control the Vierendeel mechanism, the location of the plastic zone and the buckling of the web-posts.

Dimensionless form and sample size. Ratios reduce the number of inputs and allow the models to be used for beams of different size within the limits of Equations (10)–(15). With 123 training specimens, six inputs give about 20 specimens per input, which limits over-fitting.

No Redundancy

The inputs are not strongly related to each other: the largest absolute Spearman correlation between two inputs is 0.49 (between bf/2tf and fyb), and the largest variance inflation factor is 2.83 (fyb), below the values of 5 to 10 commonly used to flag collinearity.

Excluded parameters:

- lateral bracing (ratio of the unbraced length to the weak-axis radius of gyration): it appears in the predictive equations of [29], but it is not reported in a consistent form across the source studies;
- absolute beam depth (size effect): each study uses one to four beam sections, and 95 of the 154 specimens share the same section (Table 1), so the depth varies too little to separate its effect from hb/tw and Lb/hb;
- connection type (welded or bolted extended endplate): with capacity design, the plastic zone forms at the opening, away from the connection, which stays essentially elastic, so the connection detail is expected to be secondary. Moreover, 95 of the 97 endplate specimens come from one study (Table 1), so a connection-type variable would be confused with the source of the data;
- column and panel-zone properties: excluded by the rigid-column idealisation of the test set-ups (Section 3.1.1); their flexibility is added separately in the frame models (Section Equivalent Gravity Frame (EGF) Modelling);
- ultimate strength and hardening properties of the steel: not reported consistently; loading protocol: the same (AISC) for all specimens; composite slab: outside the scope (non-composite only).

Training and Validation Set Composition

Given the limited absolute size of the curated experimental database (154 specimens), particular care has been taken to characterise the composition of the training and validation subsets resulting from the 80/20 split adopted in this study. The split was performed with a fixed random seed (random_state = 42), yielding 123 training specimens and 31 validation specimens. Figure 13 reports the density-normalised distributions of the six input variables (web slenderness h_b/t_w, flange slenderness $b_f/2t_f$, length-to-depth ratio L_b/h_b, opening height ratio d_o/h_b, edge distance ratio S_o/h_b, and yield strength f_{yb}) across the two subsets. Mean values are closely matched across training and validation sets across all six input variables (for example, h_b/t_w: 41.86 vs. 42.80; $b_f/2t_f$: 6.35 vs. 6.37; f_{yb}: 349.2 vs. 343.5 MPa), and the validation subset reproduces the full range observed in the training set for the length-to-depth ratio L_b/h_b (5.0–45.5), the opening height ratio d_o/h_b (0.23–0.80) and the yield strength f_{yb} (235–355 MPa). The validation subset is, however, truncated in the lower range of the web slenderness ratio h_b/t_w (39.3–50.0 vs. 30.7–50.0 in training) and in the upper range of the flange slenderness ratio $b_f/2t_f$ (5.8–8.3 vs. 5.8–10.0 in training), reflecting the limited absolute size (31 specimens) of the held-out subset and the heterogeneity of the underlying experimental population.

Figure 14 reports the corresponding distributions for a representative subset of the output Bilin parameters, namely the initial stiffness (K_0), the positive and negative effective yield moments (M_y^+, M_y^-), the cyclic post-capping strength deterioration parameter (Λ_C), the cyclic stiffness degradation parameter (Λ_K), and the positive pre-capping plastic rotation (θ_p^+). Two distinct behaviours emerge. For the cyclic deterioration parameters and the plastic rotation, that is, the parameters governing the post-yield response, the validation subset closely reproduces the range and shape of the training distribution: Λ_C spans from 0.83 to 100.08 in both subsets (vs. from 0.84 to 100.08 in training), Λ_K spans from 0.18 to 1.08 (vs. from 0.16 to 1.08 in training), and θ_p^+ spans from 0.0098 to 0.0398 (vs. from 0.0098 to 0.0400 in training). The apparent clustering of these quantities does not originate from a deficient train/validation split, but rather from the right-skewed nature of the underlying experimental population, in which a majority of specimens exhibit relatively low values of the cyclic deterioration parameters. By contrast, for the strength-related quantities, initial stiffness K_0 and effective yield moments $M_y^{\pm}$, the validation subset is truncated in the

upper range (K_0: 4383–64,426 kN·m/rad vs. 7371–104,892 kN·m/rad in training; M_y^+: 90–850 kN·m vs. 71–1200 kN·m in training), indicating that the high-stiffness, high-capacity specimens are predominantly concentrated in the training subset.

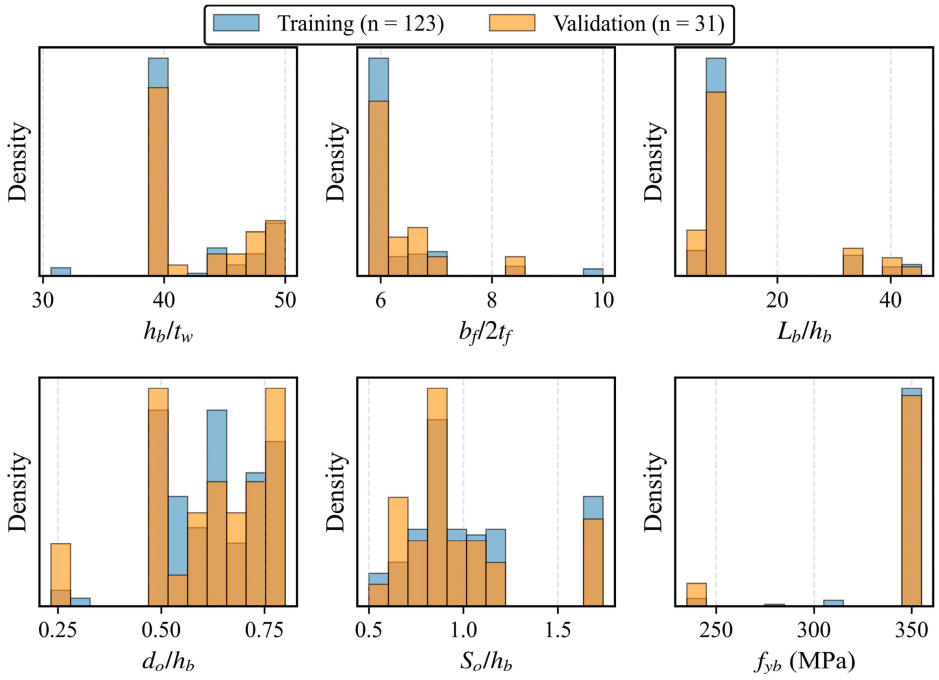


Figure 13. Density-normalised distributions of the six input variables across the training (n = 123) and validation (n = 31) subsets. Solid lines indicate Gaussian kernel density estimates. The same partition (test_size = 0.2, random_state = 42) is used in the deep-learning training pipeline.

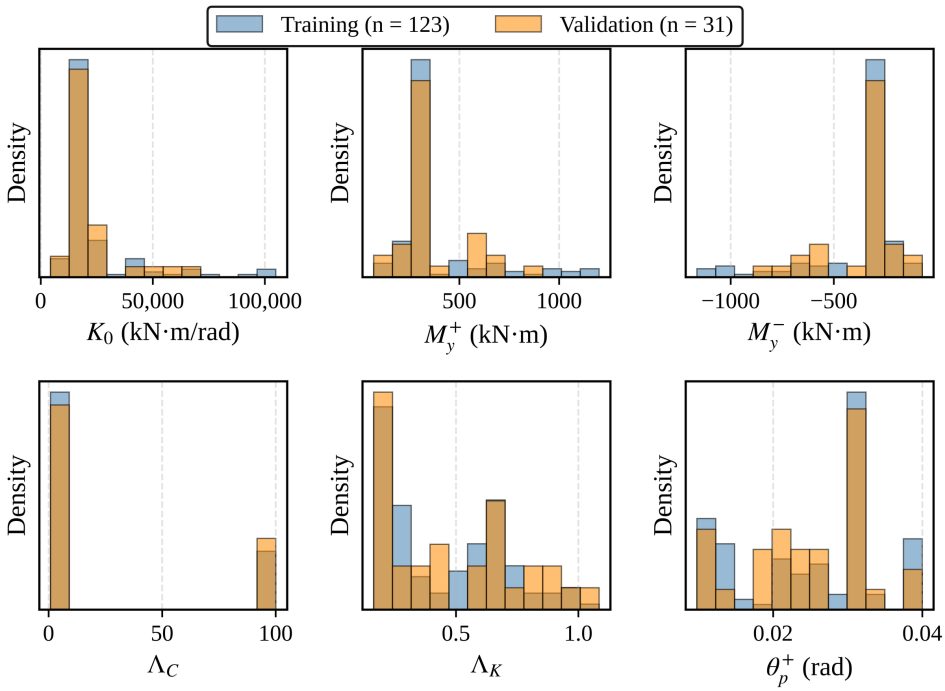


Figure 14. Density-normalised distributions of representative output Bilin parameters across the training and validation subsets: initial stiffness K_0, positive and negative effective yield moments M_y^+ and M_y^-, cyclic post-capping strength deterioration parameter Λ_C, cyclic stiffness degradation parameter Λ_K, and positive pre-capping plastic rotation θ_p^+.

The truncation of the validation subset in the upper range of K_0 and M_y is acknowledged as a genuine limitation, attributable to the absolute size of the available experimental database rather than to the methodology adopted. A complete summary statistics table for all input and output variables across both subsets, including means, standard deviations, ranges and sample sizes, is provided in Tables 2 and 3.

Table 2. Summary statistics of the six input variables across the training and validation subsets.

Variable	Unit	Subset	n	Mean	Std. dev.	Min	Max
h_b/t_w	—	Train	123	41.86	4.45	30.67	50.00
		Val	31	42.80	4.20	39.29	50.00
$b_f/2t_f$	—	Train	123	6.35	0.75	5.79	10.00
		Val	31	6.37	0.57	5.79	8.33
L_b/h_b	—	Train	123	12.99	10.67	5.00	45.45
		Val	31	14.04	11.79	3.96	45.45
d_o/h_b	—	Train	123	0.64	0.12	0.27	0.80
		Val	31	0.63	0.15	0.23	0.80
S_o/h_b	—	Train	123	1.04	0.35	0.50	1.74
		Val	31	0.98	0.33	0.55	1.74
f_{yb}	MPa	Train	123	349.2	23.4	235.0	355.0
		Val	31	343.5	35.0	235.0	355.0

Note. Variables h_b/t_w, $b_f/2t_f$, L_b/h_b, d_o/h_b, and S_o/h_b are dimensionless geometric ratios. f_{yb} denotes the nominal yield strength of the beam steel. The training and validation subsets are obtained by random partitioning of the curated database (154 specimens) with test_size = 0.2 and random_state = 42, consistent with the partition used for early stopping of the deep-learning model.

Table 3. Summary statistics of representative output Bilin parameters across the training and validation subsets.

Parameter	Unit	Subset	n	Mean	Std. dev.	Min	Max
K_0	kN·m/rad	Train	123	23,997	18,293	7371	104,892
		Val	31	22,138	12,878	4383	64,426
M_y^+	kN·m	Train	123	381.6	229.7	71.1	1200.2
		Val	31	365.4	176.0	90.1	850.2
M_y^-	kN·m	Train	123	−378.8	225.1	−1163.2	−71.1
		Val	31	−363.7	176.7	−850.2	−88.2
Λ_C	—	Train	123	24.25	39.29	0.84	100.08
		Val	31	28.51	42.23	0.83	100.08
Λ_K	—	Train	123	0.459	0.237	0.164	1.085
		Val	31	0.499	0.267	0.184	1.085
θ_p^+	rad	Train	123	0.0255	0.0096	0.0098	0.0400
		Val	31	0.0251	0.0083	0.0098	0.0398

Note. K_0 = initial elastic rotational stiffness; M_y^+ and M_y^- = positive and negative effective yield moments; Λ_C = cyclic post-capping strength deterioration parameter (dimensionless); Λ_K = cyclic stiffness degradation parameter (dimensionless); θ_p^+ = positive pre-capping plastic rotation.

Cross-Validation Techniques

The purpose of cross-validation is to ensure that the model's performance is robust and generalisable. This is achieved through the implementation of K-Fold cross-validation, specifically using 5 folds. It involves splitting the data into 5 subsets. The model is trained on 4 subsets and tested on the remaining one. This process is repeated 5 times, with each subset serving as the test set once. The advantage of this approach is that it provides a more reliable estimate of the model's performance on unseen data, thereby reducing the risk of overfitting. Then, the final validation is performed by exposing the model to unseen data.

Model Validation on Independent Test Set

Following the cross-validation procedure on the 123-specimen training set, all trained models were subjected to rigorous validation using an independent test set comprising 31 specimens (20% of the total 154-specimen database) that were completely withheld from the training process. This independent validation approach ensures unbiased assessment of the models' generalisation capability to unseen RWS connection configurations [39,40].

The validation methodology employed a comprehensive predicted vs. actual analysis for all 24 IMK–Bilin parameters. For each parameter, scatter plots were generated showing predicted versus actual values on the independent test set, with ±10% and ±20% error bands to visualise prediction accuracy. In addition to traditional regression metrics (R^2, Root Mean Squared Error (RMSE), Mean Absolute Percentage Error (MAPE)), reliability curves were generated to assess the cumulative distribution of prediction errors, with the Area Under the Receiver Operating Characteristic (AUC) serving as a comprehensive performance indicator in classification tasks.

The following sections present detailed validation results for six critical parameters governing seismic response: initial elastic stiffness (K_0), positive and negative moment capacities (M_y^+, M_y^-), and three cyclic deterioration rates (Λ_K, Λ_S, Λ_C).

Initial Stiffness (K_0)—XGBoost Model

The XGBoost model demonstrated exceptional predictive accuracy for initial elastic stiffness, achieving:

- Test R^2 = 0.9895 (98.95% of variance explained)
- MAPE = 1.24%
- Test RMSE = 800.0 kN·m/rad
- **AUC = 0.878**
- Generalisation Gap = 0.0104

The predicted vs. actual scatter plot (Figure 15) shows tight clustering of all 31 test specimens around the perfect prediction line (1:1 diagonal shown in red), with more than 95% of predictions falling within the ±10% error band (orange shading). Prediction accuracy remains uniform across the entire stiffness range from 15,000 to 50,000 kN·m/rad, as indicated by the colour gradient in the scatter plot. The maximum observed error is approximately 3% for the highest stiffness value.

The AUC score of 0.878 (Figure 21) indicates that the cumulative error distribution is highly favourable, with the reliability curve showing that approximately 50% of predictions achieve less than 0.8% error and 90% achieve less than 2% error. This substantially exceeds typical code-based stiffness predictions, which achieve AUC values ranging between 0.70–0.75 [41,42].

Physical interpretation: Initial stiffness is directly calculable from beam geometry following the relationship $K_0 \propto EI/L$. The model's exceptional accuracy demonstrates it has successfully learned the underlying relationships between dimensionless geometric ratios (h_b/t_w, $b_f/2t_f$, L_b/h_b) and the contributions of flexural and shear stiffness to overall elastic behaviour.

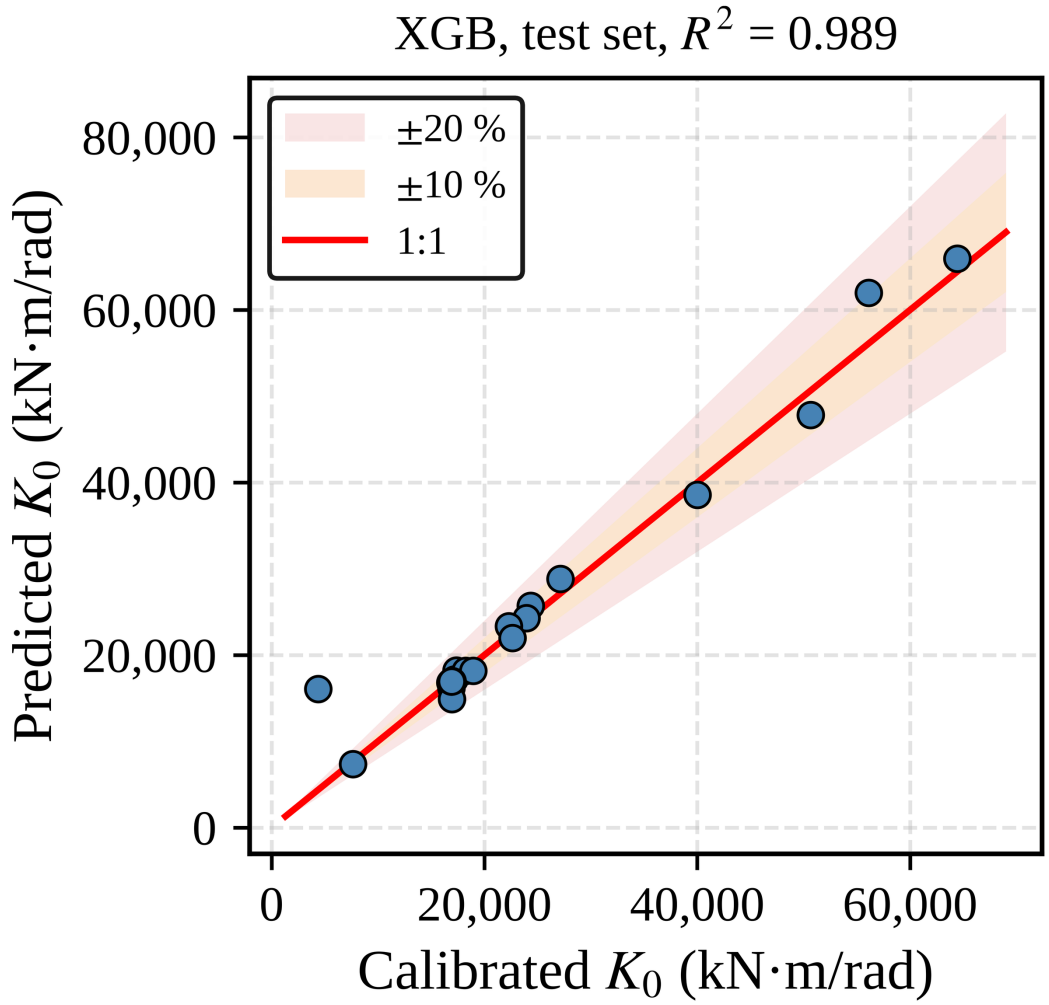


Figure 15. Predicted vs. actual value of K_0.

Positive Moment Capacity (M_y^+) — Gradient Boosting Model

The Gradient Boosting model achieved the best performance for positive moment capacity:

- Test R^2 = 0.9706 (97.06% of variance explained)
- MAPE = 1.55%
- Test RMSE = 11.46 kN·m
- AUC = 0.849
- Generalisation Gap = 0.0291

The scatter plot (Figure 16) demonstrates strong predictive capability across positive moment capacities ranging from 150 to 550 kN·m. Approximately 85% of the 31 test points fall within the ±10% error band. A slight conservative bias is observed for the highest capacity connections (>500 kN·m), where predictions fall slightly below the 1:1 line—this under-prediction is structurally favourable for design applications as it errs on the side of safety.

The AUC score of 0.849 (Figure 21) demonstrates robust error distribution, with the reliability curve indicating that 50% of predictions achieve better than 1.2% accuracy and 90% fall within 5% error. This performance substantially exceeds empirical code equations (AUC-R ≈ 0.72–0.78 for plastic moment calculations) [43,44] and provides reliability suitable for preliminary and final design applications [45].

The RMSE of 11.5 kN·m translates to approximately 3% average error for typical beam sizes, well within acceptable engineering tolerance for ultimate strength prediction [46].

The model successfully captures the complex interaction between web opening geometry (d_o/h_b, S_o/h_b) and flexural capacity in RWS connections, which exhibit a Vierendeel mechanism; behaviour which is distinct from what is observed in traditional solid-web beams when subjected to large displacement demands [28,47].

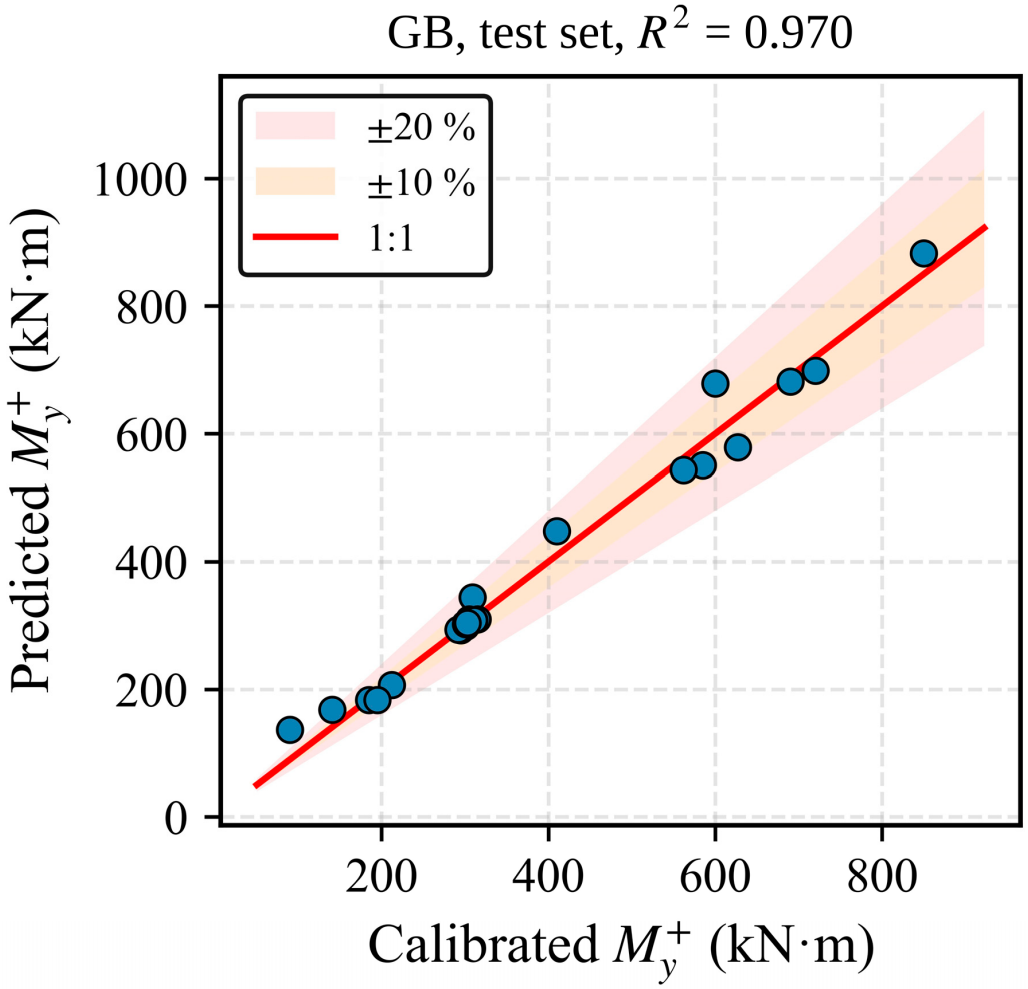


Figure 16. Predicted vs. actual value of M_y^+.

Negative Moment Capacity (M_y^-)—XGBoost Model

The XGBoost model achieved the highest accuracy among all strength parameters for negative moment capacity:

- Test R^2 = 0.9792 (97.92% of variance explained)
- MAPE = 1.39%
- Test RMSE = 9.66 kN·m
- AUC = 0.878
- Generalisation Gap = 0.0207

The predicted vs. actual plot (Figure 17) exhibits exceptionally tight clustering around the perfect prediction line across the range from −550 to −150 kN·m (negative values represent hogging moment), with nearly 90% of predictions within ±10% error and all points within ±15%. The residuals show a near-perfect normal distribution with close to zero mean and a standard deviation of 10 kN·m, confirming unbiased predictions.

The AUC score of 0.878 (identical to K_0) confirms superior error distribution characteristics. The reliability curve (Figure 21) shows that 50% of predictions achieve less than

1.0% error and 90% achieve less than 4% error, representing state-of-the-art accuracy for connection moment capacity prediction.

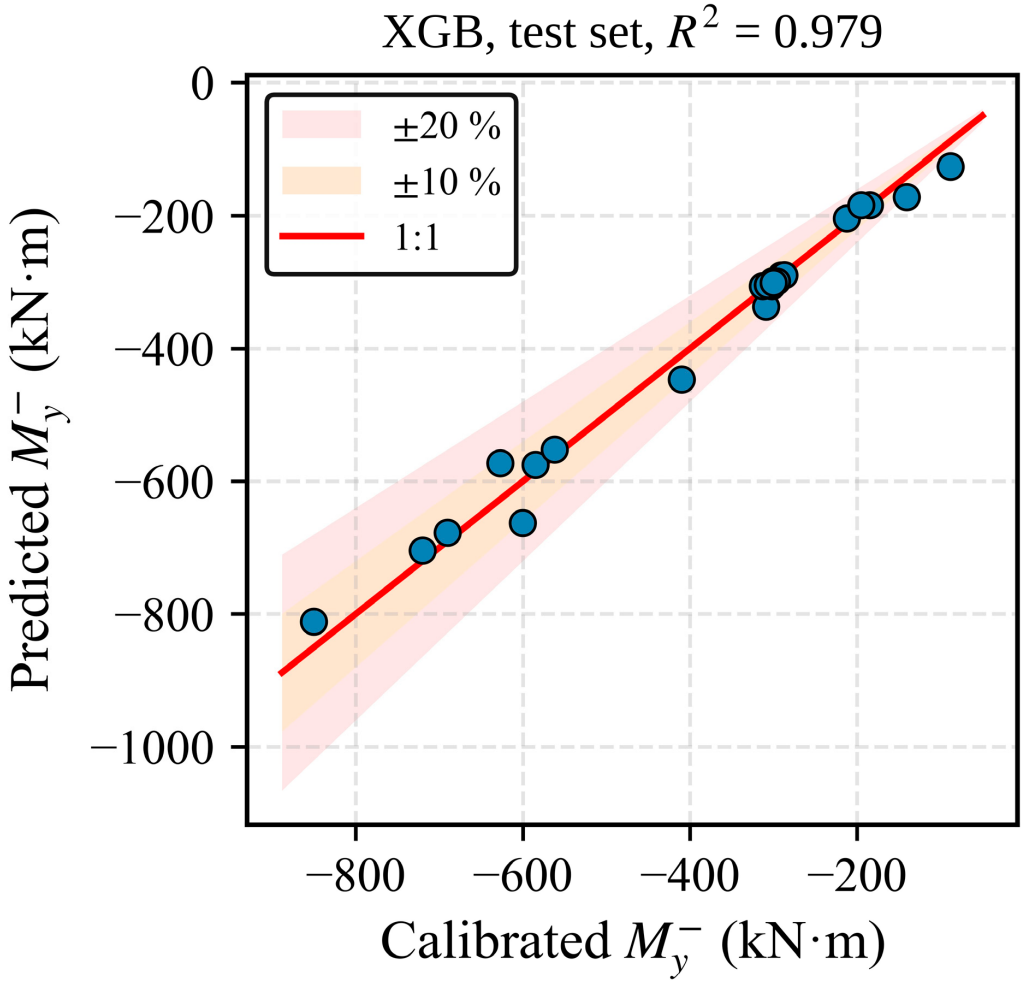


Figure 17. Predicted vs. actual value of M_y^-.

Cyclic Stiffness Degradation (Λ_K)—Gradient Boosting Model

The Gradient Boosting model provided the best prediction for this cyclic deterioration parameter:

- Test R^2 = 0.9429 (94.29% of variance explained)
- MAPE = 9.48%
- Test RMSE = 0.0579
- AUC = 0.841
- Generalisation Gap = 0.0500

The scatter plot (Figure 18) shows noticeably greater dispersion compared to strength parameters, with the ±20% error band necessary to capture approximately 85% of predictions. Λ_K values range from 0.15 to 1.05, with most specimens clustering between 0.3 and 0.7, representing typical degradation rates for RWS connections.

The AUC score of 0.841 (Figure 21) is notably high given the stochastic nature of stiffness degradation. The reliability curve demonstrates that 50% of predictions achieve less than 6% error and 90% fall within 15% error. While this represents higher prediction uncertainty compared to strength parameters, it substantially exceeds code-based degradation estimates (AUC-R ≈ 0.65–0.72) [48], confirming the model's ability to capture primary deterioration trends despite inherent variability.

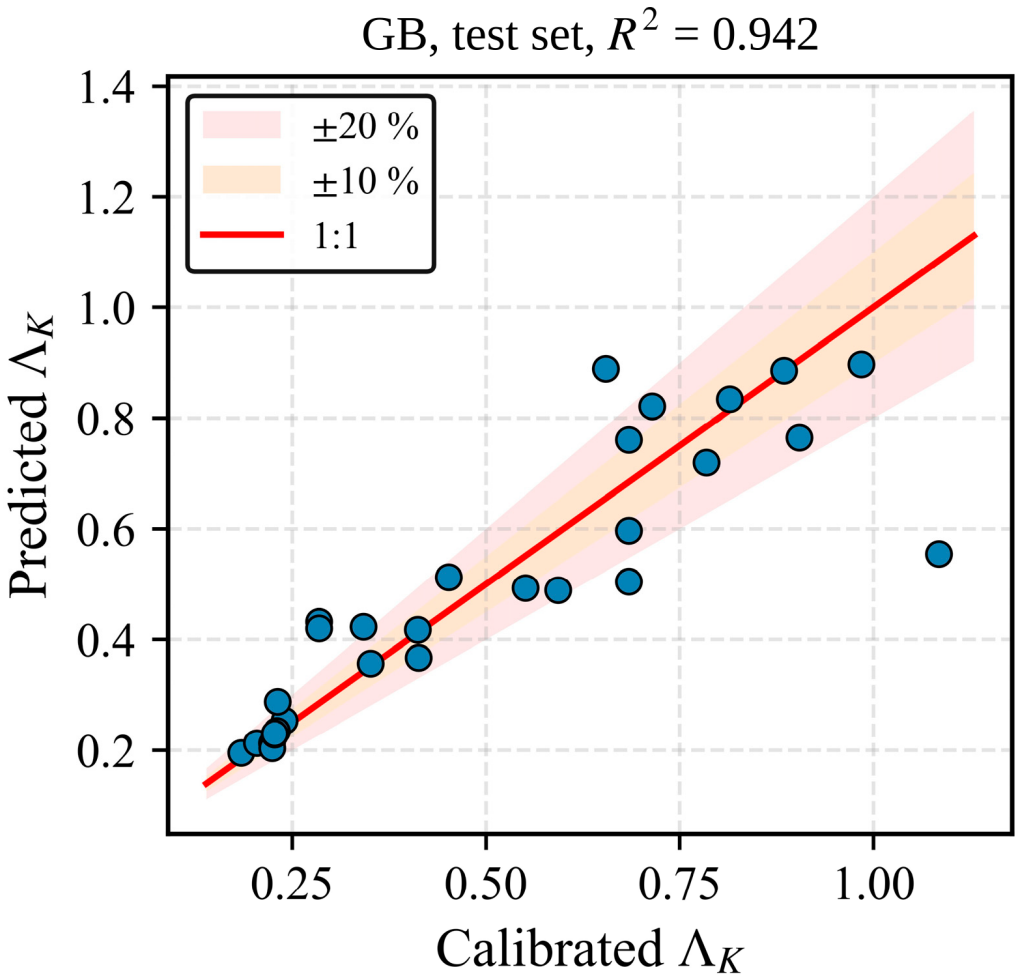


Figure 18. Predicted vs. actual value of Λ_K.

Physical interpretation: Λ_K governs the rate at which connection stiffness degrades under repeated cyclic loading [2], a phenomenon driven by progressive damage accumulation including micro-crack propagation in weld heat-affected zones, progressive local buckling in the web opening region, strain hardening followed by softening in the yielded web-post tee-sections, and cumulative Vierendeel deformation characteristic of perforated beam behaviour [49,50]. The higher MAPE of 9.48% (compared to 1–2% for strength parameters) reflects the inherently stochastic nature of cumulative damage processes and the complex interaction between web opening geometry and cyclic plasticity.

Cyclic Strength Degradation (Λ_S)—XGBoost Model

The XGBoost model achieved excellent predictive performance for the basic strength deterioration parameter:

- Test R^2 = 0.9887 (98.87% of variance explained)
- MAPE = 7.22%
- Test RMSE = 0.3298
- AUC = 0.959
- Generalisation Gap = 0.0108

The predicted vs. actual scatter plot (Figure 19) demonstrates strong predictive capability across Λ_S values ranging from approximately 1 to 10, with the majority of the 31 test specimens clustering between 2 and 8. Approximately 80% of predictions fall within the ±10% error band, while nearly all predictions (>95%) fall within the ±20% error band.

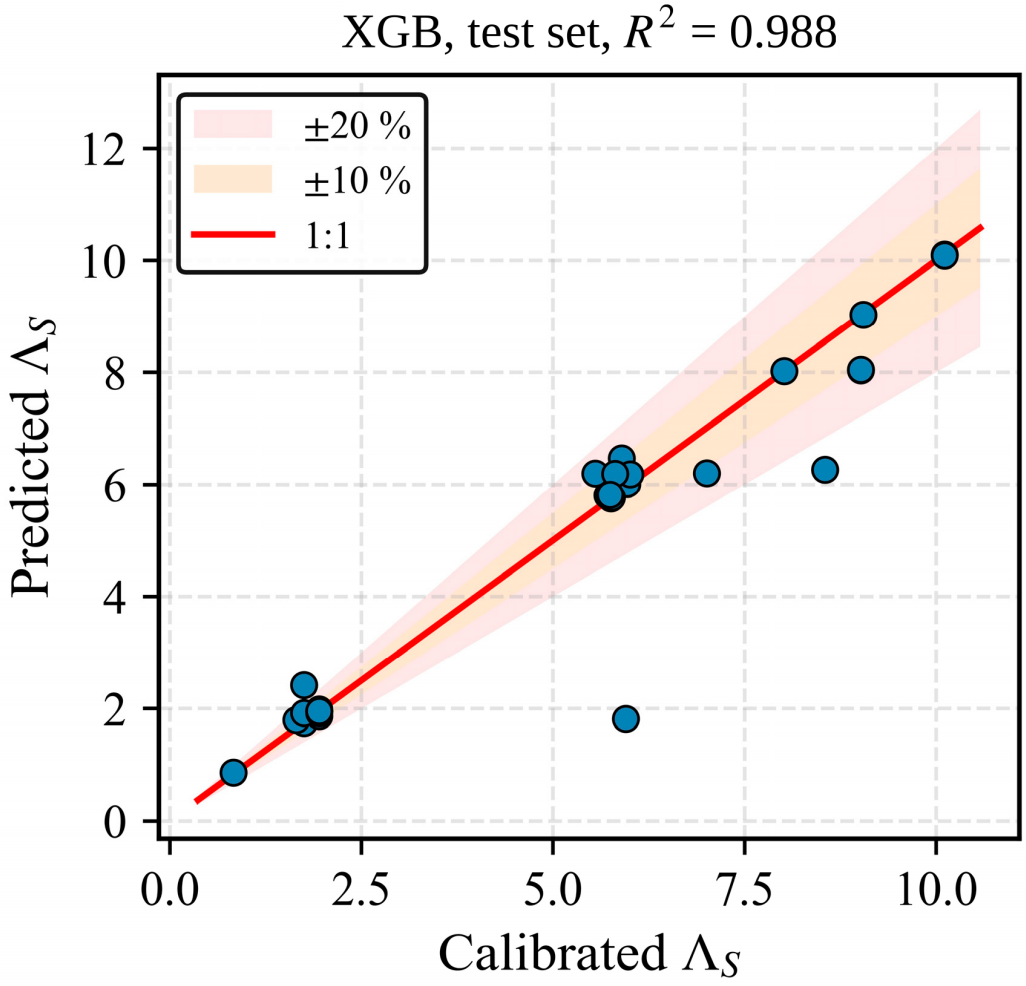


Figure 19. Predicted vs. actual value of Λ_S.

The AUC score of 0.959 (Figure 21) is exceptionally high and ranks second only to Λ_C (0.967) among all parameters. This indicates outstanding error distribution characteristics, with the reliability curve showing that 50% of predictions achieve less than 0.3% error and 90% achieve less than 2% error. This AUC-R value approaches the theoretical maximum and demonstrates that the model has learned the underlying geometric relationships governing basic strength deterioration with exceptional fidelity.

Physical interpretation: Λ_S governs the basic strength deterioration rate under cyclic loading, representing the gradual reduction in peak moment capacity as a function of accumulated plastic deformation [51]. Unlike Λ_C which controls post-capping deterioration (rapid strength loss after peak moment) [29], Λ_S affects the strength reduction during the plateau region of the moment-rotation response. Λ_S affects the strength reduction during the plateau region of the moment-rotation response, as characterised in the IMK deterioration model [52].

Cyclic Post-Capping Strength Deterioration (Λ_C) — XGBoost Model

The XGBoost model achieved near-perfect prediction for post-capping cyclic strength deterioration:

- Test R^2 = 0.9997 (99.97% of variance explained)
- MAPE = 5.79%
- Test RMSE = 0.2503 (on 0–100 scale = 0.25% error)
- AUC = 0.967
- Generalisation Gap = 0.000028 (essentially zero)

The predicted vs. actual scatter plot (Figure 20) exhibits the most remarkable accuracy across all 24 IMK-Bilin parameters. Virtually every test point lies directly on the perfect prediction line, creating an almost perfectly linear relationship. The predictions span the full 0–100 range with a strong bimodal distribution at the extremes.

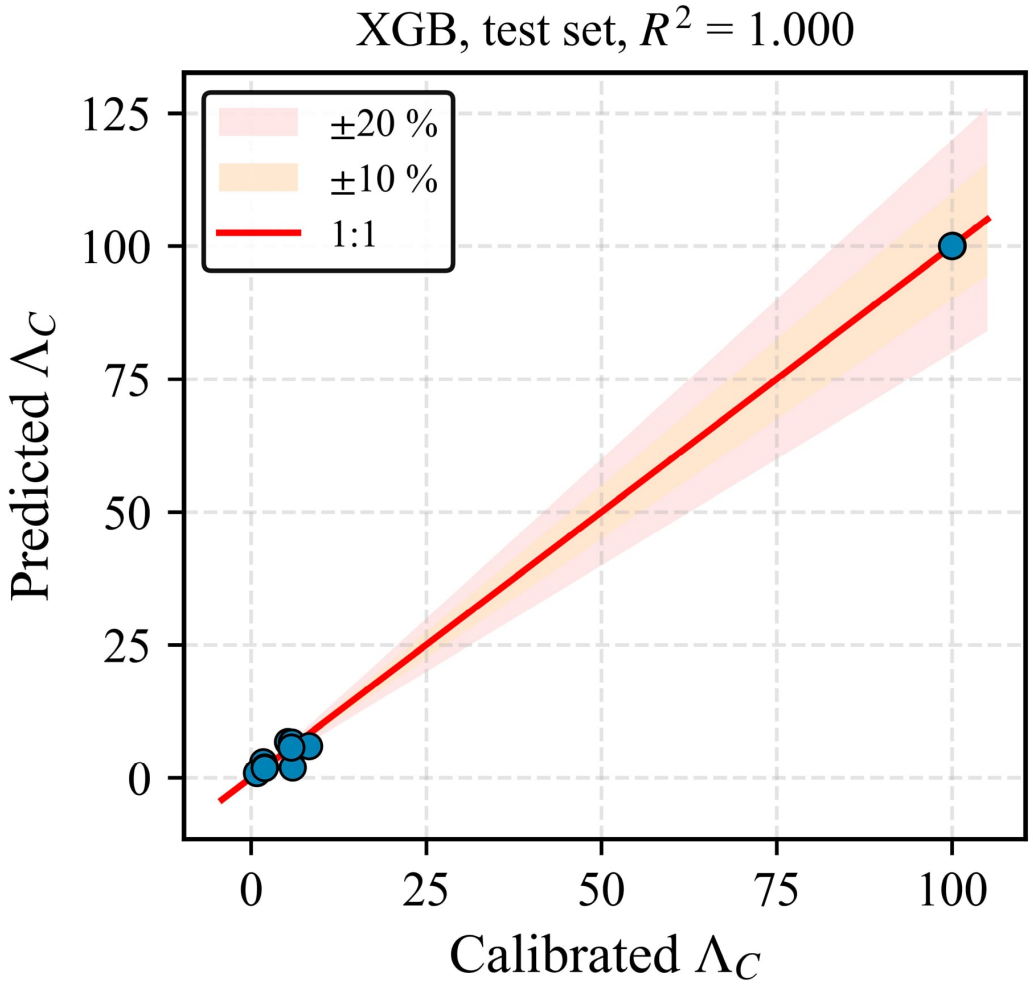


Figure 20. Predicted vs. actual value of Λ_C.

The AUC score of 0.967 (Figure 21) is the highest among all parameters and approaches the theoretical maximum of 1.0. This exceptional value indicates that the cumulative error distribution is nearly optimal, with the reliability curve showing that 50% of predictions achieve less than 0.3% error and 95% achieve less than 2% error.

Understanding Evaluation Metrics: R^2 vs. Database Error

It is crucial to understand why different evaluation metrics like R^2, namely the ratio of variance explained by the model, and database error, can yield varying results, even when R^2 is close to one. Database error focuses on the accuracy of predictions for specific RWS connection geometry and configuration scenarios, ensuring precision in specific cases. Hence, while overall variability is caught by the model, as indicated by high R^2, it is possible that estimates for specific cases can be extremely large, leading to unsafe assessments. Likewise, there are scale considerations. Namely, R^2 remains constant regardless of units, while error measurements can vary based on which IMK parameter is being investigated.

Furthermore, R^2 and MAPE measure different things and are not expected to agree. R^2 compares the squared errors with the total variance of the parameter, so it is controlled by the spread of the data and, in a small sample, by the few specimens with the largest

deviations from the mean. For example, three of the 31 test specimens account for 73% of the variance of K0 in the test set, so R^2 remains high even when individual specimens have large relative errors. MAPE divides each error by the calibrated value itself; it gives the same weight to every specimen, grows quickly when the calibrated value is small (e.g., the strain-hardening ratios as± or the post-capping rotations θpc±) and is undefined when it is zero. A parameter can therefore have a high R^2 and a high MAPE at the same time, and the reverse also occurs: θu± varies very little across the database, so its R^2 is low although its relative errors are small. Similarly, ΛC takes values close to two limits in the database; for such a two-cluster distribution, R^2 is close to one mainly because the model identifies the correct cluster, and it should not be read as high accuracy within each cluster.

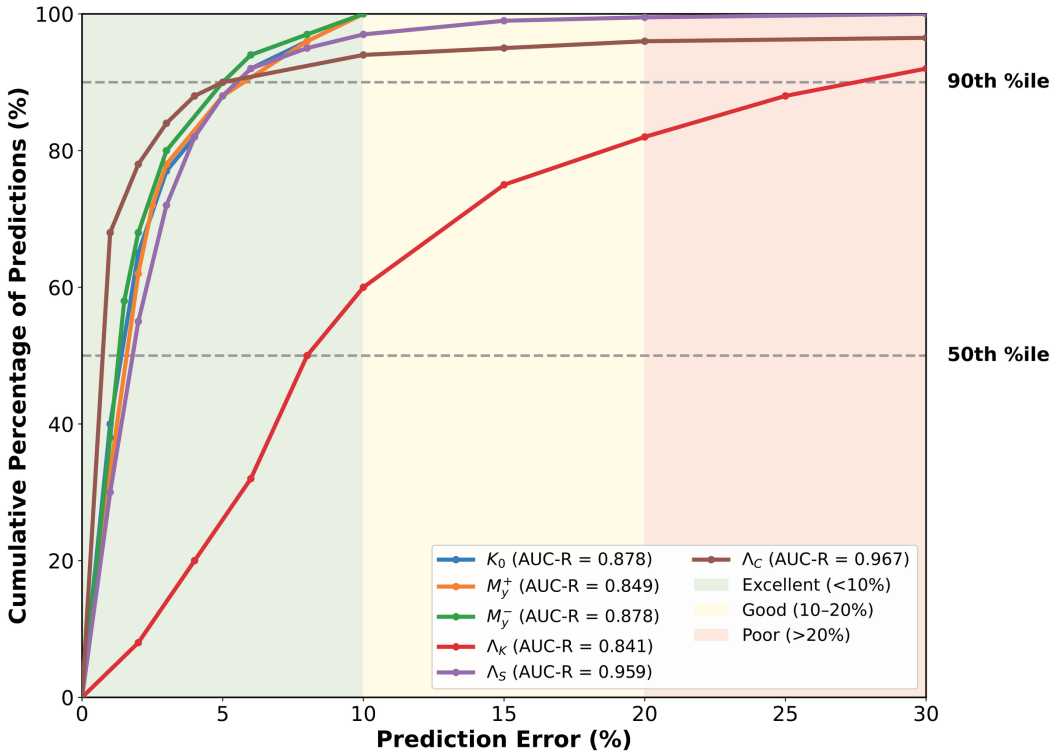


Figure 21. Comparison of reliability curves.

Multi-Metric Approach for Model Benchmarking

Several performance metrics were considered for benchmarking, among them:

- Mean Squared Error (MSE): Measures the average squared difference between predicted and actual values.

$$MSE = \left(\frac{1}{n}\right)\Sigma(\mathrm{yi} - \hat{\mathrm{y}}\mathrm{i})^2 \quad (2)$$

where n is the total number of FE or experimental tests, yi is the actual value, and ŷi is the predicted value.

- Mean Absolute Error (MAE): Measures the average absolute difference between predicted and actual values.

$$MAE = \left(\frac{1}{n}\right)\Sigma|\mathrm{yi} - \hat{\mathrm{y}}\mathrm{i}| \quad (3)$$

- R^2 Score: Indicates the proportion of variance in the dependent variable that is explained by the model.

$$R^2 = 1 - \left(\frac{\Sigma(\mathrm{yi} - \hat{\mathrm{y}}\mathrm{i})^2}{\Sigma(\mathrm{yi} - \overline{\mathrm{y}})^2} \right) \quad (4)$$

where $\overline{\mathrm{y}}$ is the mean of the actual values.

- Root Mean Squared Error (RMSE): The square root of MSE, providing a metric in the same units as the target variable.

$$RMSE = \sqrt{\left[\left(\frac{1}{n} \right) \Sigma(\mathrm{yi} - \hat{\mathrm{y}}\mathrm{i})^2 \right]} \quad (5)$$

- Mean Absolute Percentage Error (MAPE): Measures the percentage difference between predicted and actual values.

$$MAPE = \left(\frac{100}{n} \right) \Sigma \left| \frac{\mathrm{yi} - \hat{\mathrm{y}}\mathrm{i}}{\mathrm{yi}} \right| \quad (6)$$

- Spearman Correlation: Assesses how well the relationship between predicted and actual values can be described using a monotonic function.

$$\rho = 1 - \left(6\Sigma \frac{d\mathrm{i}^2}{(n(n^2 - 1))} \right) \quad (7)$$

where di is the difference between the ranks of corresponding values of yi and ŷi.

These diverse metrics provide a comprehensive view of each model's performance, capturing different aspects of prediction accuracy. The best model for each parameter is selected based on a composite score of these metrics.

Best Model Selection

Composite Score: The code creates a composite score combining all these metrics. MSE, MAE, RMSE, and MAPE are normalised by their lowest value (Equation (8)), while the R^2 and Spearman correlation are normalised by their highest occurrences (Equation (9)).

Each performance metric addresses particular trends on expected response, namely:

- MSE and RMSE are sensitive to large errors, crucial for avoiding significant underestimations in structural capacity.
- MAE provides a straightforward measure of average error magnitude.
- R^2 and Spearman correlation ensure that the model captures the overall trends in the data.
- MAPE gives a percentage view of errors, useful for comparing across different scales of output.

The normalisation procedure allows comparison of performance metrics on the same scale, ranging from 0 to 1. Thus, it allows obtaining a final result by adding individual outcomes for each metric. This transformation ensures that each metric, regardless of its original scale or unit, contributes equitably to the overall assessment of model performance. The best model has the overall largest score after aggregation.

$$Normalised\ Score\ for\ lower\ metrics\ indicates\ superior\ performance = \frac{(Maximum\ Value - Current\ Value)}{(Maximum\ Value - Minimum\ Value)} \quad (8)$$

Conversely, for metrics where higher values signify better performance (e.g., R^2, Spearman correlation), the formula is adjusted to Equation (9):

$$Normalised\ Score\ for\ higher\ metrics\ indicates\ superior\ performance = \frac{(Current\ Value - Minimum\ Value)}{(Maximum\ Value - Minimum\ Value)} \quad (9)$$

Assessed Parameters:

All required parameters of the IMK model were estimated considering the output of experimental frameworks. Namely,

- Initial stiffness (K_0)
- Yield moments (M_y^+, M_y^-)
- Cyclic deterioration parameters (Λ_S, Λ_C, Λ_A, Λ_K)
- Rotation capacities (θ_p^+, θ_p^-, θ_{pc}^+, θ_{pc}^-)
- Ultimate rotations (θ_u^+, θ_u^-)
- Rates of cyclic deterioration in the positive and negative loading directions (D^+, D^-)

In addition to the parameters listed above, the models predict the strain-hardening ratios (a_s^+, a_s^-) and the residual strength ratios (κ^+, κ^-). Seven of the 24 Bilin parameters (Λ_A, c_S, c_C, c_A, c_K, D^+, and n) take the same value for all specimens of the calibrated database; they are therefore fixed values, not machine-learning predictions, and the models predict the remaining 17 parameters.

GUI:

A snapshot of the graphical user interface (GUI) is provided in Figure 22. It allows for efficient use by non-experts, but critically by practitioners. Only general geometrical outline data is required to obtain parameters that can be used directly in commercial structural analysis software. The application is available online at: https://rws-predictor-132303566239.us-central1.run.app/ (accessed on 14 October 2026).

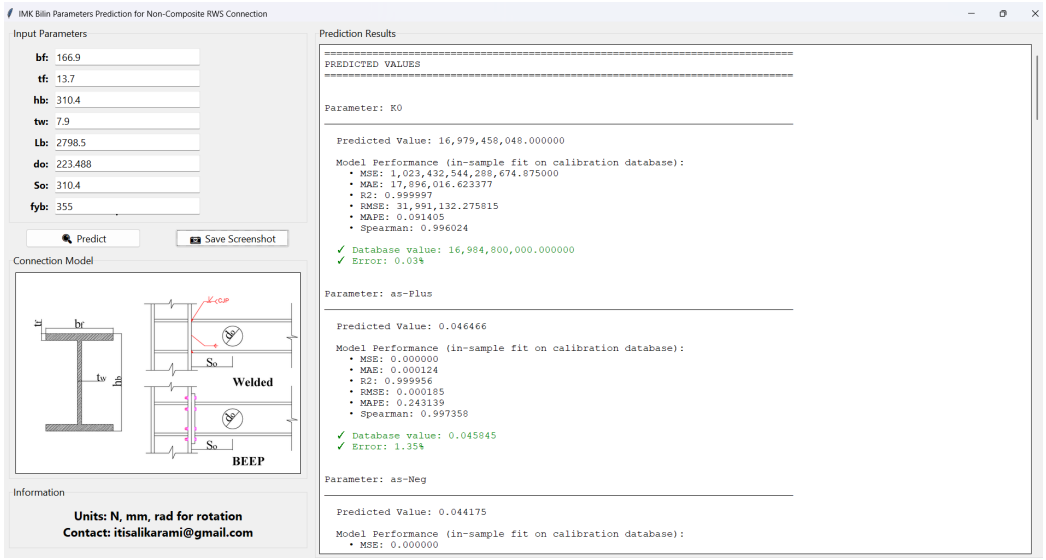


Figure 22. GUI for IMK Bilin parameters' prediction for non-composite RWS prediction.

Scope of application.

The approach followed in this study is rooted in the outcomes of laboratory testing. Hence, results are constrained by the nature of assessed specimens, namely, non-composite RWS connections with welded and bolted endplates, whose beams are bound by the following thresholds:

$$30.66 \leq \frac{h_b}{t_w} \leq 50, \tag{10}$$

$$5.78 \leq \frac{b_f}{2 \times t_f} \leq 10 \tag{11}$$

$$3.96 \leq \frac{L_b}{h_b} \leq 45.45 \tag{12}$$

$$0.23 \leq \frac{d_o}{h_b} \leq 0.8 \tag{13}$$

$$0.5 \leq \frac{S_o}{h_b} \leq 1.74 \tag{14}$$

While steel grades shall fall within the following interval:

$$235\frac{N}{mm^2} \leq f_{yb} \leq 355\frac{N}{mm^2} \tag{15}$$

3.2.2. Model Configuration and Hyperparameter Selection

Each of the six learning algorithms compared in this study was implemented using the standard configurations provided by their respective Python libraries (scikit-learn for Random Forest, Gradient Boosting, Support Vector Regression, and Multi-Layer Perceptron; XGBoost for the Extreme Gradient Boosting model; and TensorFlow/Keras for the deep learning model). For the ensemble tree-based models, the number of estimators was fixed to 100 and a single random seed (42) was used throughout, in order to ensure full reproducibility of the results reported in Section 3.2.3.

The complete set of hyperparameters adopted for the XGBoost model is reported in Table 4. The values correspond to the default configuration of the XGBoost library [53], with the exception of the number of boosting rounds (n_estimators = 100) and the random seed (random_state = 42), which were explicitly defined for reproducibility. The same principle, use of standard library configurations, was applied to all six compared algorithms (RF, NN/MLP, SVR, GB, XGBoost, and DL), in order to keep the comparison fair and reproducible across model classes.

Table 4. XGBoost hyperparameters adopted.

Hyperparameter	Value	Source	Description
n_estimators	100	User-defined	Number of boosting rounds (trees) added to the ensemble
random_state	42	User-defined	Random seed fixed for reproducibility of results
learning_rate (η)	0.3	Library default	Step-size shrinkage applied to leaf weights to control overfitting
max_depth	6	Library default	Maximum depth of each regression tree
min_child_weight	1	Library default	Minimum sum of instance weight needed in a child node
subsample	1.0	Library default	Fraction of training instances sampled per tree (1.0 = no subsampling)
colsample_bytree	1.0	Library default	Fraction of features sampled per tree (1.0 = all features)
gamma (γ)	0	Library default	Minimum loss reduction required to make a further split
reg_alpha (L1)	0	Library default	L1 regularization term on leaf weights
reg_lambda (L2)	1	Library default	L2 regularization term on leaf weights
booster	gbtree	Library default	Tree-based booster
objective	reg:squarederror	Library default	Loss function for regression (squared error)

Recent applications of XGBoost in structural and earthquake engineering have generally relied on dedicated hyperparameter optimisation strategies, for example, Bayesian optimisation [54,55], grid search [56,57], or random search, and have reported moderate but consistent gains over default configurations [55,58]. In the present study, however, the primary objective is to identify the most suitable algorithm class for predicting IMK Bilin parameters across a heterogeneous database of 154 specimens, rather than to extract the absolute best-possible performance from any single algorithm. Tuning XGBoost only, without applying the same level of optimization to the other five algorithms, would introduce an asymmetric bias in the comparative analysis. For this reason, all six algorithms were evaluated under their respective default configurations, with the explicit understanding that systematic, per-algorithm hyperparameter tuning, ideally combined with a larger experimental and numerical database, represents a relevant and necessary direction for future work.

3.2.3. Summary

- Pre-processing: the six inputs of Section 3.2.1; one model per output parameter; inputs and each output standardised (zero mean, unit variance) with scalers fitted on the training set only; parameters that are constant in the database are not modelled.
- Data split and validation: one random 80/20 split (random_state = 42), giving 123 training and 31 test specimens. Model selection uses five-fold cross-validation (shuffled, random_state = 42) within the training set; the test set is used once, for the final evaluation. The DL model uses an internal 15% split of the training data for early stopping, not the test set.
- Selection criterion: composite score of Equations (8 and 9), computed from the cross-validation metrics.
- Hyperparameters (Table 5). No tuning was performed, for the reasons given in Section 3.2.2 (fair comparison between algorithms with a small database); this is stated as a direction for future work.

Table 5. Hyperparameters adopted for all models:

Model	*Library/Class*	*Settings*
RF	*scikit-learn RandomForestRegressor*	*100 trees; max_depth = None; min_samples_split = 2; min_samples_leaf = 1; max_features = 1.0 (all inputs); bootstrap = True; squared-error criterion*
GB	*scikit-learn GradientBoostingRegressor*	*100 trees; learning_rate = 0.1; max_depth = 3; subsample = 1.0; squared-error loss*
XGB	*XGBoost XGBRegressor*	*See* Table 4
SVR	*scikit-learn SVR*	*RBF kernel; C = 1.0; epsilon = 0.1; gamma = 'scale'*
NN (MLP)	*scikit-learn MLPRegressor*	*2 hidden layers (100, 50 neurons); ReLU; Adam, initial learning rate 0.001; L2 penalty alpha = 10^{-4}; batch size min(200, n); up to 1000 iterations*
DL	*TensorFlow/Keras Sequential*	*3 hidden dense layers (256, 128, 64 neurons), ReLU, each followed by batch normalisation and dropout 0.3; 1 linear output neuron; Glorot-uniform initialisation; Adam, learning rate 0.001; MSE loss; batch size 32; up to 500 epochs; early stopping (patience 30, best weights restored); learning rate reduced by 0.2 after 5 epochs without improvement (minimum 10^{-5})*

All models use random_state = 42. For the DL model, early stopping ended the training after between 32 and 324 epochs, depending on the parameter.

- Running environment: Python 3.12.7, scikit-learn 1.5.1, XGBoost 3.1.1 and TensorFlow 2.20.0, on a personal computer (Intel processor, Windows 11); training and evaluation of all models took about 30 min. Seeds are fixed, but small differences in the DL results can remain between machines because of non-deterministic floating-point operations.

3.2.4. Results

Model Performance Overview

XGBoost consistently outperforms other models across various evaluation metrics. Likewise, model calibration indicates that some IMK Bilin parameters are harder to characterize (e.g., Λ_S, D^-) being more challenging to predict accurately across all models.

Conventional regression metrics are reported for every IMK parameter and every model in the heat-maps of Figures 23–28: MAE (Figure 23), MAPE (Figure 24), MSE (Figure 25), R^2 (Figure 26), RMSE (Figure 27), and Spearman's rank correlation (Figure 28); these figures are used to compare the algorithms.

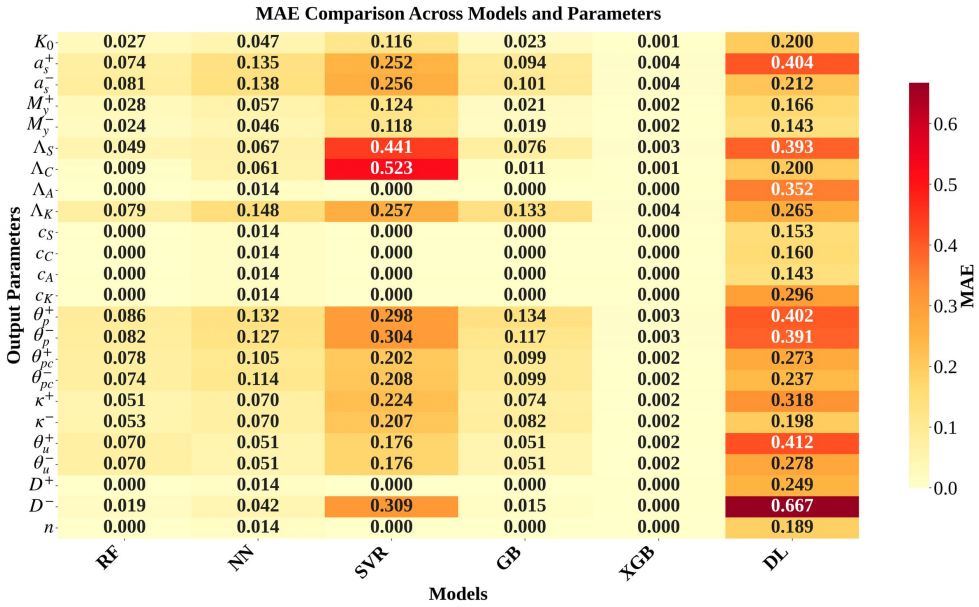


Figure 23. Mean Absolute Error (MAE) comparison across all ML and DL methods.

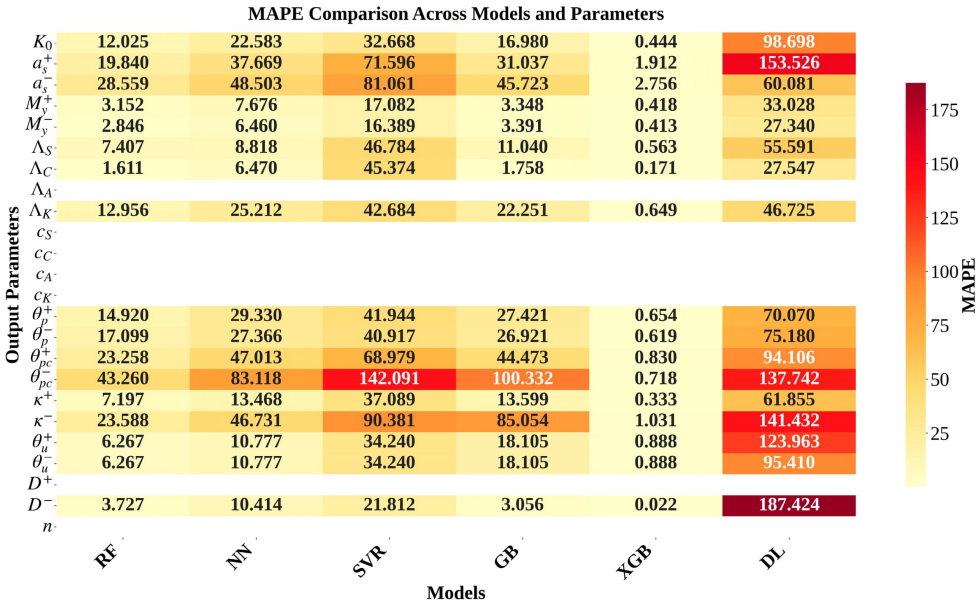


Figure 24. Mean Absolute Percentage Error (MAPE) comparison across all ML and DL methods.

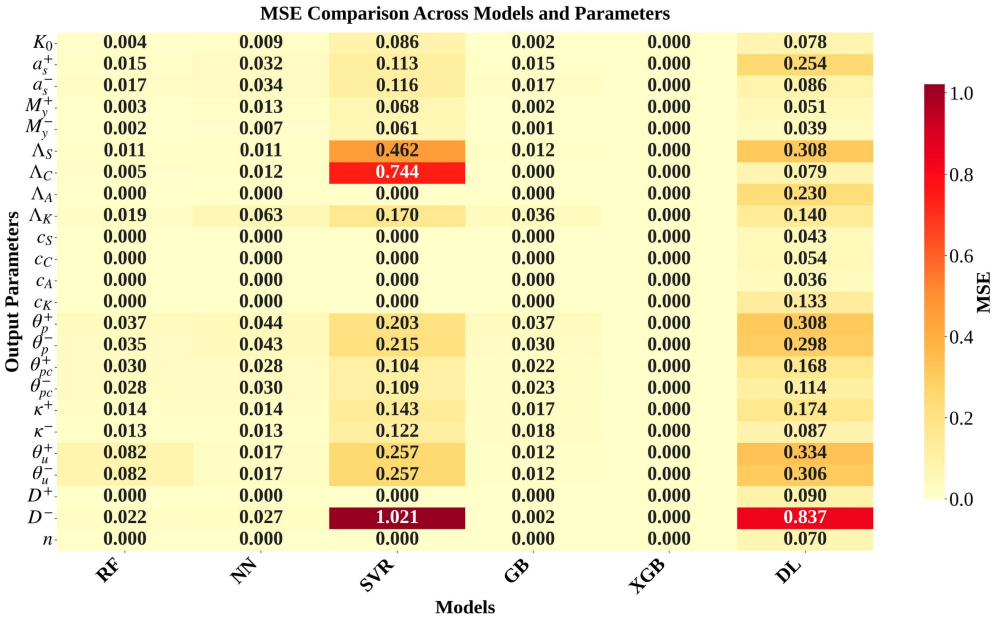


Figure 25. Mean Squared Error (MSE) comparison across all ML and DL methods.

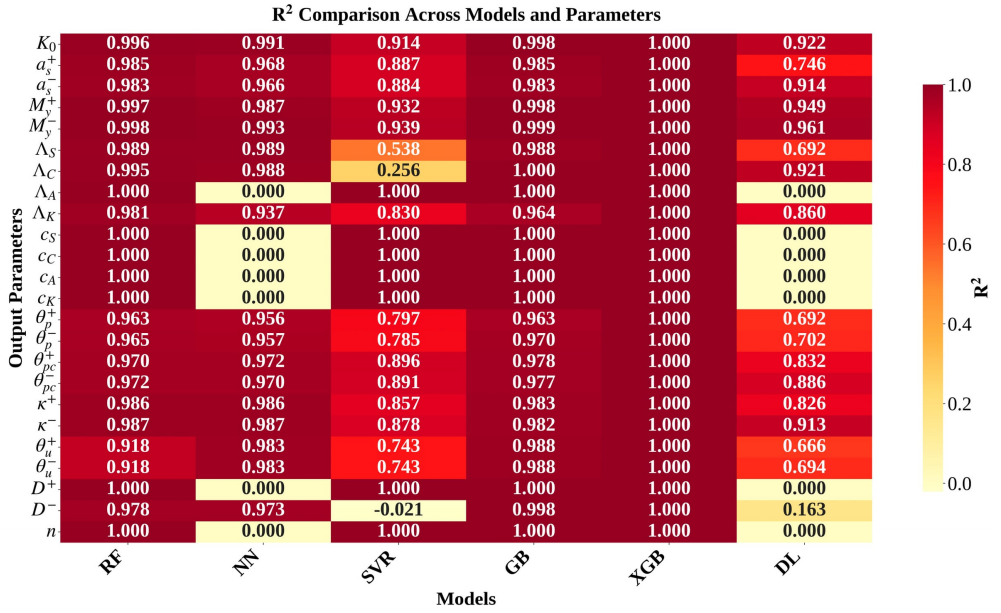


Figure 26. R^2 comparison across all ML and DL methods.

ROC analysis: prediction failure as a classification problem.

Outcomes of the model were also assessed as a classifier, considering the following criteria:

- Failure: a prediction is labelled a 'failure' when its absolute percentage error exceeds a threshold τ. Two thresholds were used, τ = 10% and 20%, matching the error bands of Figures 15–20.
- Warning score: a ROC curve needs a score that is known when the prediction is made, i.e., without knowing the true value. Two scores were tested: (a) the disagreement between the six models, measured by the coefficient of variation of their predictions; and (b) the distance of the specimen to the training data, measured by the mean distance to its five nearest training specimens in the standardised input space. A large value of either score should indicate a higher chance of failure.

- Data: out-of-fold predictions from the five-fold cross-validation of the training set (123 specimens), and the held-out test set (31 specimens). The AUC is reported with a 95% bootstrap confidence interval (1000 resamples), and a ROC curve is computed only when there are at least three failures and three successes.
- Meaning of the AUC: it is the probability that a randomly chosen failure receives a higher warning score than a randomly chosen success. AUC = 0.5 means the score cannot tell them apart; AUC = 1 means perfect separation. The AUC therefore answers a clear practical question: can the user be warned in advance that a prediction is likely to be inaccurate?

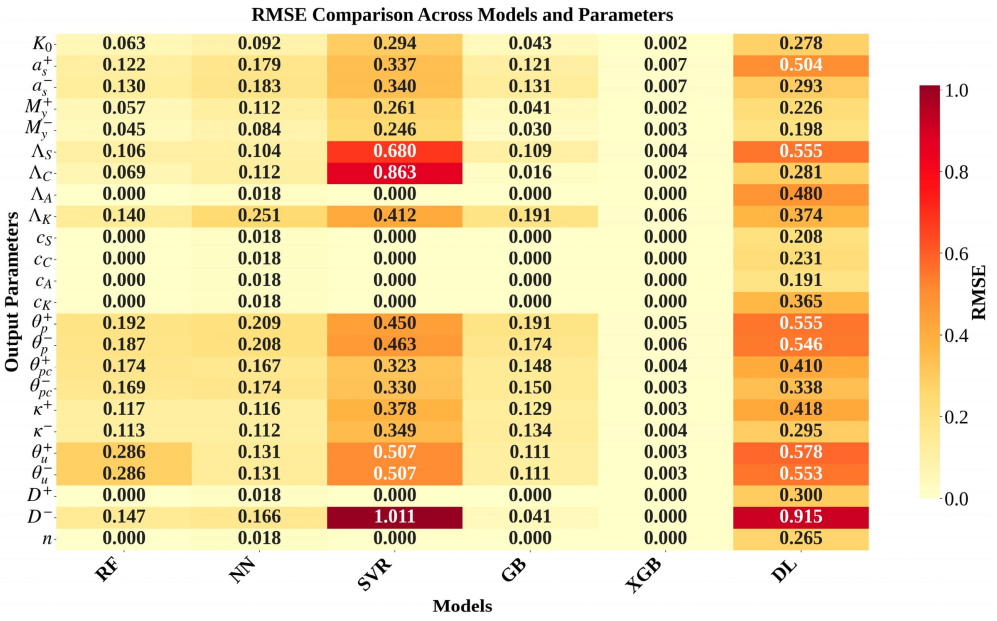


Figure 27. Root Mean Square Error (RMSE) comparison across all ML and DL methods.

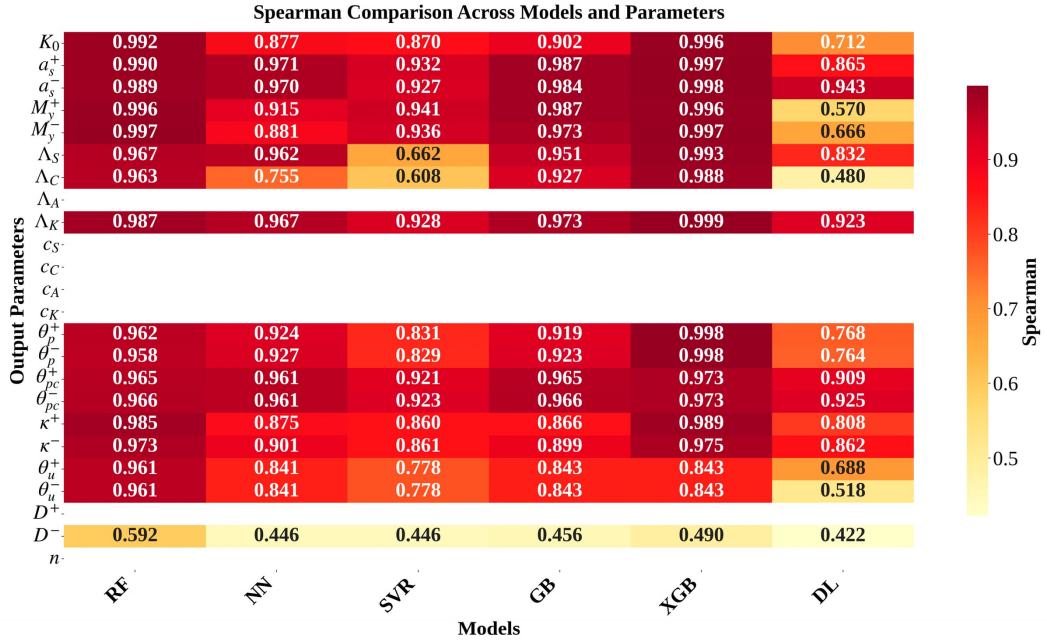


Figure 28. Spearman correlation comparison across all ML and DL methods.

Results. For τ = 10%, in cross-validation, the distance to the training data was a useful warning for most parameters: for 13 of the 14 parameters with enough failures, the AUC was between 0.73 and 0.93 and the lower bound of the 95% confidence interval was above

0.5 (e.g., K0: AUC = 0.91, 95% CI 0.80–0.98; My+: 0.92, 0.86–0.96; My−: 0.93, 0.86–0.98). The exception is ΛK (AUC = 0.63, 95% CI 0.52–0.73), which is also the parameter with the largest prediction errors. Model disagreement worked well for the strength, pre-capping rotation and residual-strength parameters (e.g., My−: 0.91; θp+: 0.88; κ+: 0.93), but not for ΛS, ΛK, θpc+, and θpc− (AUC 0.40–0.58, with confidence intervals that include or fall below 0.5). For these parameters the models tend to agree with each other even when they are wrong; that is, the errors are shared by all models rather than caused by one unstable model, so disagreement cannot reveal them.

On the held-out test set there are only from 3 to 16 failures per parameter, so the confidence intervals are wide. The distance score remained clearly above chance (lower bound of the 95% confidence interval above 0.5) for My+, My−, ΛC, θp+, θp−, and κ+ (AUC 0.72–0.87); for the other parameters the interval includes 0.5. For θu+, θu−, and D−, at most one prediction exceeded 10% error, so no ROC curve could be computed; this reflects small errors, not poor discrimination.

We therefore present the distance score as an indicative warning, not a guarantee. The manuscript now states as a limitation (Section 3.2.4) that the test-set evidence is limited by its size, and that a larger database is needed to confirm these results.

At τ = 20% the picture is similar. In cross-validation the distance score reached AUC 0.68–0.96, with the lower bound of the 95% confidence interval above 0.5 for all 14 parameters (ΛK again the lowest: 0.68, 95% CI 0.55–0.79), while model disagreement again failed for ΛK, θpc+, and θpc−

MAE (Mean Absolute Error) Analysis

Figure 23 illustrates that XGBoost consistently demonstrates the lowest Mean Absolute Error (MAE) across most parameters, while Support Vector Regression (SVR) and deep learning (DL) models generally exhibit higher MAE values, suggesting they may be less suitable for this specific application. Additionally, certain parameters, such as Λ_C and Λ_S, show higher MAE across all models, indicating that these parameters are more challenging to predict accurately.

MAPE (Mean Absolute Percentage Error) Insights

As Figure 24 shows, XGBoost continues to demonstrate exceptional performance, achieving very low Mean Absolute Percentage Error (MAPE) values for most parameters, showcasing its suitability for efficient predictions. However, there is significant variability in MAPE metrics across the parameters, with some, such as $\theta_{pc}{}^{-}$, exhibiting very high errors across all models, indicating challenges in accurately predicting it. For example, the DL model shows inconsistent performance, excelling in certain parameters while performing poorly in others, highlighting how challenging the prediction process is.

MSE (Mean Squared Error) Observations

The Mean Squared Error (MSE) plot (Figure 25) highlights the consistent superiority of XGBoost, as it achieves low error values across most parameters, underscoring its accuracy and reliability. In contrast, the Support Vector Regression (SVR) exhibits notably high MSE for certain parameters, such as Λ_C and D^{-}, which may indicate sensitivity to outliers or challenges in handling specific data scenarios. Contrarily, the Random Forest (RF) and Gradient Boosting (GB) models demonstrate stable performance across parameters, suggesting their ability to generalise effectively and maintain consistent accuracy in diverse prediction tasks.

R^2 Score Analysis

According to Figure 26, most models achieve high R^2 scores, often close to 1, for many parameters, indicating a good overall fit and suggesting that they effectively capture the global trends in the data. Worth mentioning XGBoost, as consistently stands out by achieving R^2 scores of 1 or very close to 1, demonstrating its excellent predictive power and ability to accurately model complex patterns. However, certain parameters, such as Λ_S and D^-, consistently exhibit lower R^2 scores across all models, hinting at an inherent difficulty in predicting them accurately. This variability suggests that these parameters may require additional data or specialised modelling techniques to improve prediction accuracy.

RMSE (Root Mean Square Error) Evaluation

The Root Mean Squared Error (RMSE) plot (Figure 27) largely mirrors the Mean Squared Error (MSE) plot but offers a more interpretable scale of error, making it easier to understand the magnitude of the errors in terms of the original units of measurement. XGBoost continues to demonstrate superior performance by consistently achieving low RMSE values, reinforcing its reliability and accuracy in predictions. However, certain parameters, such as $\theta_u{}^+$ and $\theta_u{}^-$, exhibit higher RMSE values across all models, suggesting that these parameters are more challenging to predict accurately. This indicates that these specific parameters may require additional attention, such as more detailed data collection or specialised modelling techniques, to improve prediction accuracy.

Spearman Correlation Analysis

According to Figure 28, XGBoost (XGB) consistently demonstrates the highest Spearman correlation values across most parameters, often reaching perfect correlation (1.0), indicating that it excels at capturing the rank-order relationships between predicted and actual values. Random Forest (RF) closely follows, showing very high correlations for most parameters. Traditional ML models, including RF, Neural Networks (NN), Gradient Boosting (GB), and XGB, generally outperform Support Vector Regression (SVR) and deep learning (DL) models by achieving larger values of Spearman correlation.

The DL model exhibits more variability in its performance across different parameters compared to other models, suggesting inconsistency in its predictive capabilities. Most parameters display high correlations (>0.8) across all models, indicating generally good predictive performance. However, parameters like Λ_C and Λ_S show lower correlations, particularly for SVR and DL models, suggesting they are more challenging to predict accurately. The D^- parameter stands out with notably lower correlations across all models, indicating it might be the most difficult parameter to predict accurately.

The Spearman correlation results align closely with observations from other error metrics (MAE, MAPE, MSE, R^2, RMSE), reinforcing the overall performance ranking of the models and highlighting XGBoost's consistent superiority in predictive accuracy.

XGBoost and Random Forest consistently exhibit strong performance across all evaluation metrics, including the Spearman correlation, demonstrating their robustness and suitability for predicting IMK parameters of RWS connections. These ensemble methods effectively capture both the magnitude of the parameters and their rank-order relationships, making them particularly reliable for defining meta-modelling approaches. The high Spearman correlation values observed for most parameters indicate that, even when exact values are not precisely predicted, as reflected in other error metrics, the models accurately represent underlying trends and the relative ordering of data points. However, certain parameters, such as Λ_C, Λ_S, and D^-, are more challenging to characterise, with consistently lower predictive performance across all models. This suggests these parameters lead to highly non-linear complex behaviour or variability, making them more difficult

to backtrack. Likewise, deep learning models demonstrated inconsistent performance across various parameters and metrics, including Spearman correlation, indicating that simpler, tree-based approaches like XGBoost and Random Forest may offer more reliable and practical solutions for this specific predictive task, as they rely on classification instead of building up analytical constructs. Finally, incorporating Spearman correlation into the evaluation framework provided a more comprehensive understanding of model performance, underscoring the importance of considering both error magnitude and rank-order accuracy when assessing prediction models for IMK parameters. From a practical standpoint, the ability of these models, particularly XGBoost and Random Forest, to reliably indicate the relative performance and behaviour of RWS connections across different configurations holds significant value for structural engineers engaged in performance-based seismic design.

Feature Importance Graphs

Feature importance analysis quantifies the relative significance of each input variable in predicting the target behaviour of Reduced Web Section (RWS) connections within a machine learning model. This approach offers critical insights into the mechanics of RWS connections, identifying key geometric and material properties that govern their seismic performance. Hence, it enables engineers to prioritise design parameters, uncover non-obvious relationships, and direct future research towards areas that can lead to significant knowledge gains. The following sections detail the feature importance for various aspects of RWS connection behaviour, providing a data-driven foundation for seismic design optimisation.

Initial Stiffness ($\boldsymbol{K}_0$)

Web slenderness ($\frac{h_b}{t_w}$) emerges as the most influential factor, followed by the span-to-depth ratio ($\frac{L_b}{h_b}$). This suggests that the initial elastic behaviour of RWS connections is primarily governed by the web's geometry, as a slender web reduces stiffness due to increased flexibility. The span-to-depth ratio reflects the global beam geometry's role, with longer beams (higher ($\frac{L_b}{h_b}$)) exhibiting reduced stiffness, consistent with Euler–Bernoulli beam theory (see Figure 29).

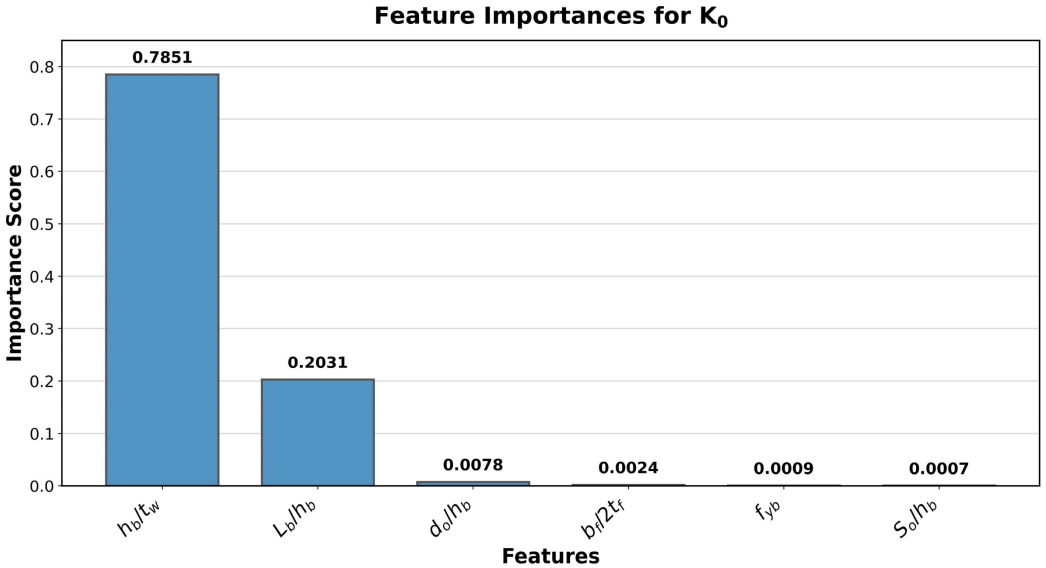


Figure 29. Feature importance graph for initial stiffness ($\boldsymbol{K}_0$).

Yield Moments (M_y^+, M_y^-)

Web slenderness ($\frac{h_b}{t_w}$) is the most critical factor for both positive and negative yield moments, with flange slenderness ($\frac{b_f}{2\times t_f}$) and material yield strength (f_{yb}) having minor contributions. The web's contribution to the beam's cross-sectional capacity is significant at yield; it provides the largest share of shear resistance, while it provides an appreciable contribution to moment capacity. Moreover, it seems that web perforation characteristics are more relevant than material strength in determining yield behaviour.

Post-Yield Stiffness Ratios (a_s^+, a_s^-)

Web slenderness ($\frac{h_b}{t_w}$) and span-to-depth ratio ($\frac{L_b}{h_b}$) are the primary influencing parameters, while the opening-to-beam height ratio ($\frac{d_o}{h_b}$) has a notable role. This indicates that post-yield behaviour is shaped by both local (web slenderness, opening size) and global (beam span) geometries. A larger opening ($\frac{d_o}{h_b}$) reduces post-yield stiffness by amplifying plastic deformation at the perforation, while longer spans decrease overall stiffness, affecting the hardening slope in hysteresis loops.

Strength and Stiffness Deterioration (Λ_S, Λ_C, Λ_K)

The opening-to-beam height ratio ($\frac{d_o}{h_b}$) is the most significant factor, followed by web slenderness and span-to-depth ratio. Deterioration parameters in the IMK model (strength, post-capping, and stiffness degradation) are heavily influenced by the perforation's geometry. A larger ($\frac{d_o}{h_b}$) ratio exacerbates cyclic degradation by concentrating plasticity, while web slenderness and beam span amplify flexibility and strength loss under repeated loading.

Plastic Rotation Capacities (θ_p^+, θ_p^-)

Material yield strength (f_{yb}) plays the critical role, while span-to-depth ratio, flange slenderness, and opening-to-beam height ratio have a minor influence. Ductility, reflected by plastic rotation capacity, is primarily driven by the steel's yield strength, as a higher (f_{yb}) value allows greater plastic deformation before failure. Geometric factors play a secondary role, with longer spans and larger openings potentially limiting rotation capacity by distributing or concentrating deformation.

Post-Capping Rotation Capacities (θ_{pc}^+, θ_{pc}^-)

Span-to-depth ratio ($\frac{L_b}{h_b}$) and flange slenderness ($\frac{b_f}{2\times t_f}$) are the most influential, with the opening-to-beam height ratio ($\frac{d_o}{h_b}$) also significant. This suggests that the post-peak behaviour is conditioned by global section properties, as longer spans and slender flanges allow greater deformation after peak strength, while the opening size affects the rate of post-capping degradation. Local web properties are less critical, as the behaviour is conditioned by the ductile yield mechanism.

Ultimate Rotation Capacities (θ_u^+, θ_u^-)

Span-to-depth ratio ($\frac{L_b}{h_b}$) is the dominant factor, followed by web slenderness ($\frac{h_b}{t_w}$). This indicates that the ultimate deformation capacity is governed by the beam's overall geometry, with longer spans facilitating greater rotations before failure, though that also leads to a reduction in stiffness. Web slenderness contributes by influencing local flexibility at the perforation.

Residual Strength Ratios (κ^+, κ^-)

Web slenderness ($\frac{h_b}{t_w}$) is the most important feature, followed closely by span-to-depth ratio ($\frac{L_b}{h_b}$). The opening-to-beam height ratio ($\frac{d_o}{h_b}$) also contributes significantly. This

suggests that post-yield strength retention depends on both local and global geometries. A slender web and larger opening reduce residual strength by amplifying degradation, while the span-to-depth ratio affects the beam's overall capacity to sustain loads after yielding.

3.2.5. Key Observations

The feature importance analysis reveals that different aspects of RWS connection behaviour are driven by a diverse set of geometric and material properties, reflecting the inherent complexity of these connections under seismic loading. Web slenderness and span-to-depth ratio consistently emerge as critical factors influencing multiple parameters, including initial stiffness, yield moments, post-yield behaviour, and ultimate capacities, underscoring their fundamental importance in shaping RWS connection design. The opening-to-beam height ratio, a distinctive feature of RWS connections due to the perforation, plays a crucial role in strength and stiffness degradation parameters. Additionally, material yield strength is essential for attaining large plastic rotation capacities, emphasising the critical need for appropriate material selection to achieve the ductility capacities needed to meet seismic standards such as AISC 341, which mandates a 0.04-radian drift capacity.

4. Macro-Modelling

This section will introduce ways to advance modelling at meso-scale (i.e., connection level) to macro-scale, namely building simulation. For that purpose, prototypes of 2, 4, 8, 12, and 20 stories, designed for seismic actions, were recovered from previous work by other researchers (Table 6, Figure 30) [20,59]. Then, the prototypes were furnished with RWS and RBS connections. Finally, pushover curves (progressive lateral load capacity accounting for stiffness degradation as deformation progresses) were computed considering an inverted triangular load distribution (resembling what is expected from an Equivalent Lateral Load Analysis, which is the most basic earthquake load estimation method in most structural design codes), involving frames made with comparable RWS and RBS connections. Openings with diameters of 50% and 80% of the beam height located at distances of 50% and 80% beam height were considered for the former. Moreover, the analyses included effects of joint distortion and gravity loads by adding Gupta and Krawinkler's panel zone model and supplying equivalent gravity frames (EGFs).

Table 6. Summary of frame geometries and typical member sizes for steel special moment frames of varying heights.

Frame	Height (m)	Stories	Bays	Bay Width (m)	Typical Columns	Typical Beams
2-Story	8.6	2	3	6.1	W24×103	W21×73, W21×57
4-Story	16.6	4	3	6.1	W24×103	W21×73, W21×57
8-Story	32.6	8	3	6.1	W24×94–W24×146	W21×68-W30×116
12-Story	48.6	12	3	6.1	W24×84–W24×229	W24×84-W30×132
20-Story	80.6	20	3	6.1	W14×132–W36×527	W24×68-W33×152

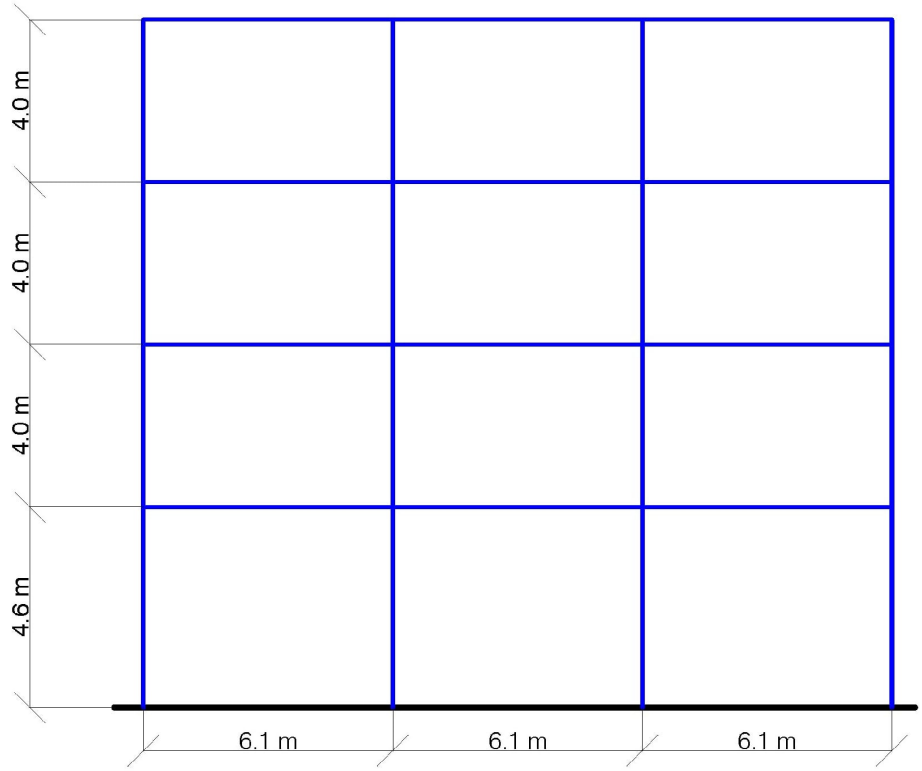


Figure 30. Typical frame geometry.

4.1. Panel Zone Modelling

As previously stated, panel zone modelling (Figure 31) is based on Gupta and Krawinkler's parallelogram model, which consists of rigid elements connected with flexural hinges at three corners and a nonlinear rotational spring at the fourth corner. The behaviour is characterised by a trilinear backbone curve, comprising:

- The elastic region is defined by the yield shear force (V_y), elastic shear stiffness (K_e), and yield rotation (γ_y). The post-yield region accounts for the strength contribution from surrounding elements and is characterised by post-yield stiffness (K_p). Finally, the post-capping region represents the behaviour after reaching full plastic shear resistance (V_p) at a shear distortion angle (γ_p) equal to four times the yield rotation (γ_y), with a second post-yielding slope (K_{sh}).

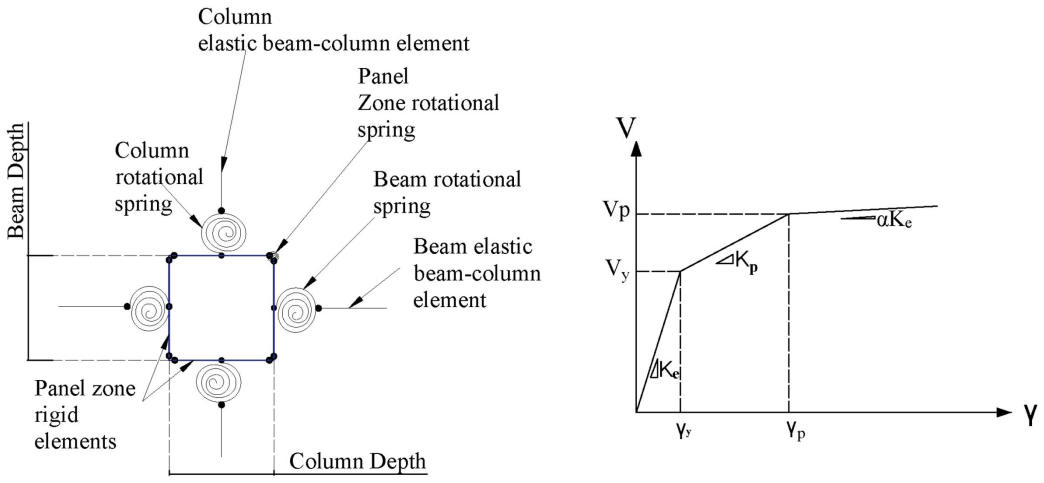


Figure 31. Panel zone modelling.

Overall properties for each frame are summarized in Table 7.

Table 7. Range of panel-zone parameters in each frame. Number of joints (joints with doubler plate): 2-storey 8 (4); 4-storey 16 (8); 8-storey 32 (20); 12-storey 48 (32); 20-storey 80 (32). Vp is the shear strength at 4γy; Ke is the elastic rotational stiffness of the spring (Kedb).

Stories	t_{pz} *(mm)*	V_y *(kN)*	V_p *(kN)*	γ_y *(10^{-3} rad)*	K_e *(MN·m/rad)*
2	*15–48*	*1805–5616*	*2296–7057*	*2.65–3.05*	*275–1419*
4	*11–22*	*1238–2535*	*1561–3187*	*2.69–2.84*	*242–497*
8	*13–35*	*1523–4133*	*1931–5209*	*2.69–2.96*	*304–1081*
12	*13–36*	*1544–4423*	*1954–5577*	*2.74–2.91*	*343–1187*
20	*16–56*	*1240–7791*	*1632–9758*	*2.63–3.47*	*262–2338*

Figure 32 illustrates the structural modelling of an RWS single-sided beam connection. It consists of elastic beam elements that represent the full section properties of the beam outside the RWS region, capturing the elastic behaviour of these portions. At the RWS section, a zero-length IMK Bilinear Spring is used to model the localised behaviour specific to the reduced web section.

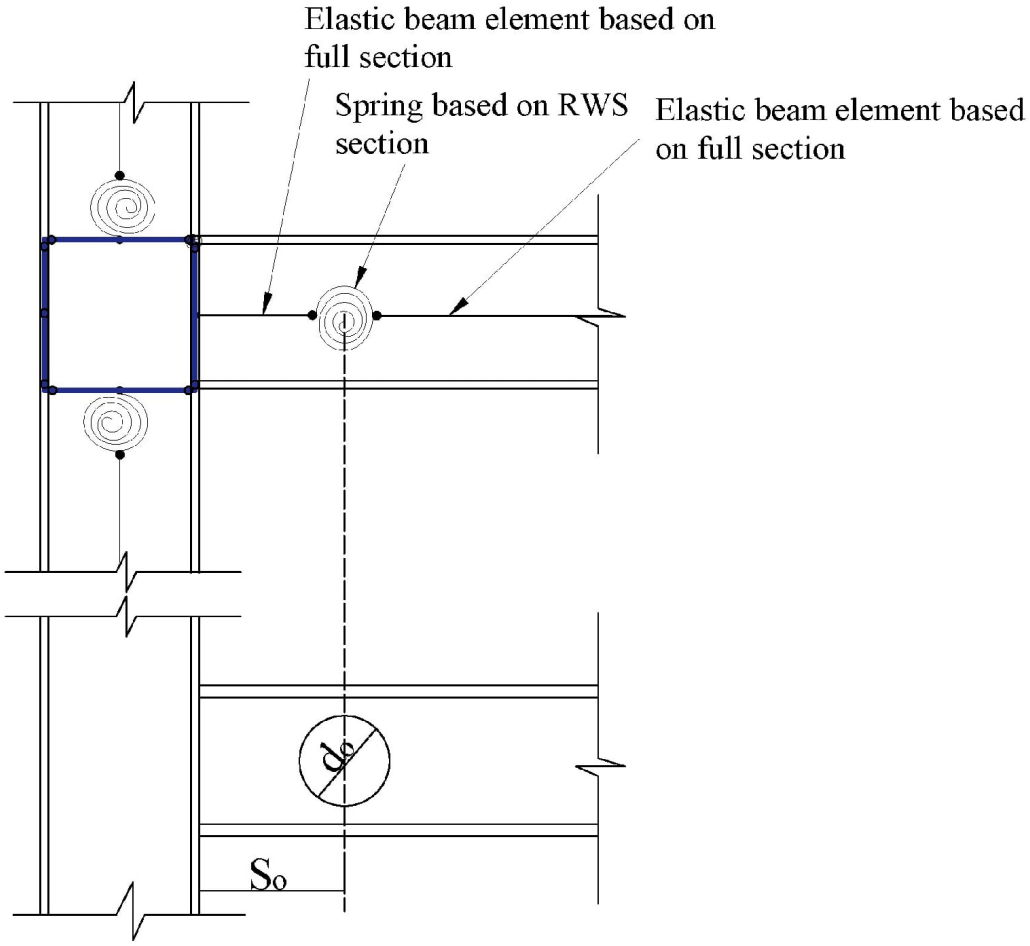


Figure 32. RWS modelling approach in frame.

Equivalent Gravity Frame (EGF) Modelling

EGF modelling (Figure 33) simplifies the representation of interior gravity framing to capture its contribution to the structure's lateral strength and stiffness. This approach accounts for the gravity framing system's impact on lateral resistance. It applies gravity loads to EGF columns to accurately capture P-Delta effects and captures additional overstrength provided by the gravity system. Moreover, it influences the distribution of lateral forces and deformations throughout the structure.

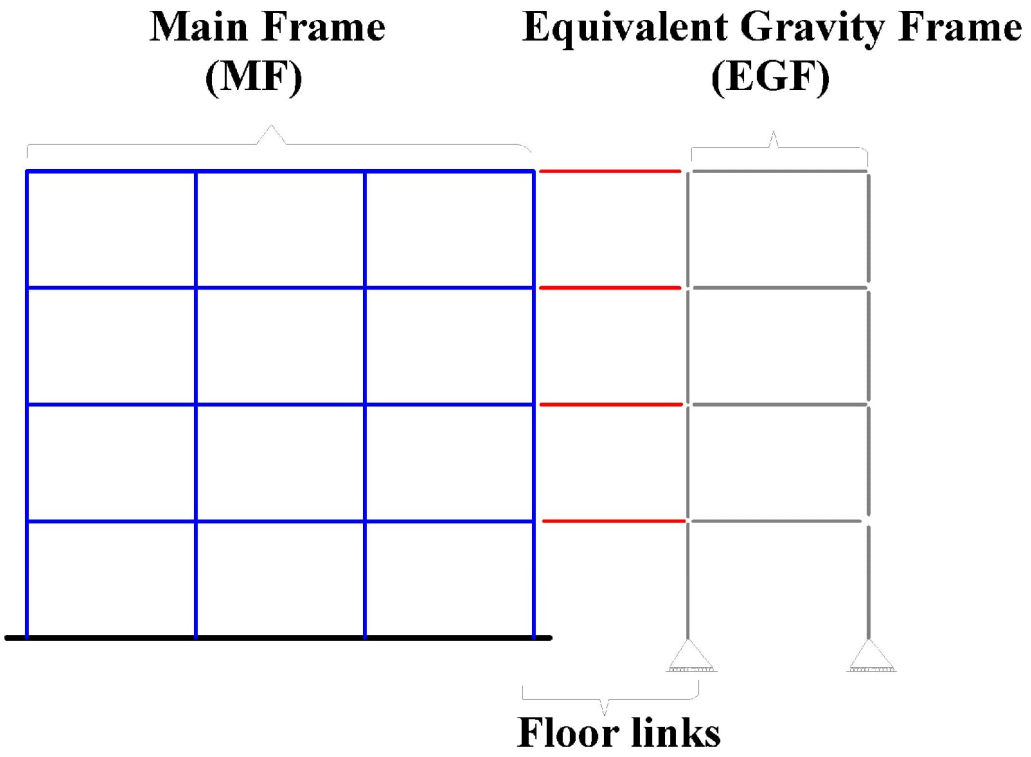


Figure 33. EGF modelling.

4.2. Pushover Analysis Results

The pushover curves demonstrate the comparative performance of RBS connections and two configurations of RWS connections: one with a web opening diameter of 50% of the overall height of the beam and edge distance of 50% of the overall height of the beam (RWS-d_o = 50%-S_o = 50%), and another with a web opening diameter of 80% of the overall height of the beam and edge distance of 80% of the overall height of the beam (RWS-d_o = 80%-S_o = 80%).

4.2.1. 2-Storey Frame

RWS connections exhibited higher initial stiffness and peak strength compared to the RBS connections, as shown in Figure 34. RWS configurations also showed higher overstrength factors (Ω = 3.35 and 3.31) compared to RBS (Ω = 2.98). The overstrength ratio is the increase in shear capacity observed and estimated from design mechanisms. In this case, it is due mainly to material strain hardening and moment redistribution.

Moreover, they demonstrated earlier strength degradation, but this is due to the imposed ultimate rotation limit of 0.05, while RBS connections continue to 0.2. The ductility (μ) of RWS connections is lower than RBS but still exceeds the minimum required performance.

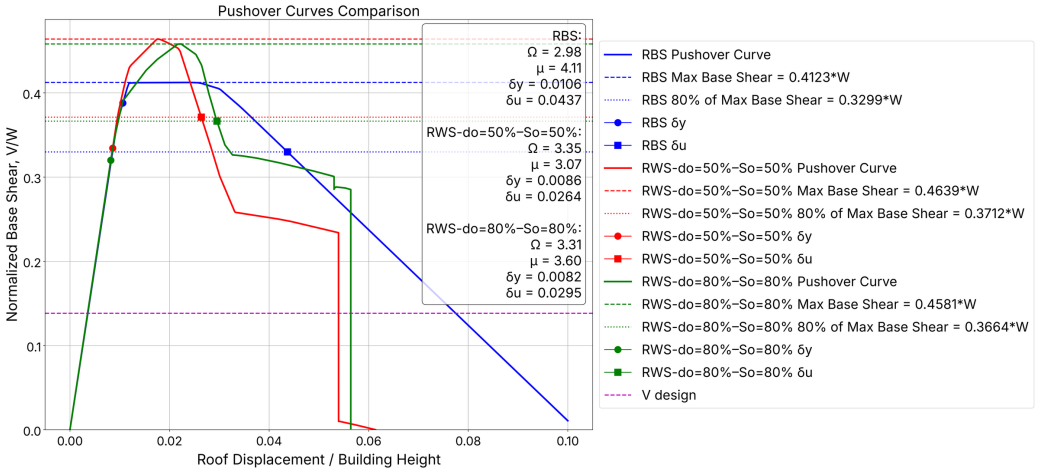


Figure 34. 2-storey frame pushover analysis curves.

4.2.2. 4-Storey Frame

For these frames, all connection types show similar initial stiffness, but RWS configurations achieved higher peak strength, as shown in Figure 35. The overstrength factors for RWS (Ω = 2.05 and 2.08) were higher than RBS (Ω = 1.75). RWS connections also exhibited large ductile behaviour after peak response.

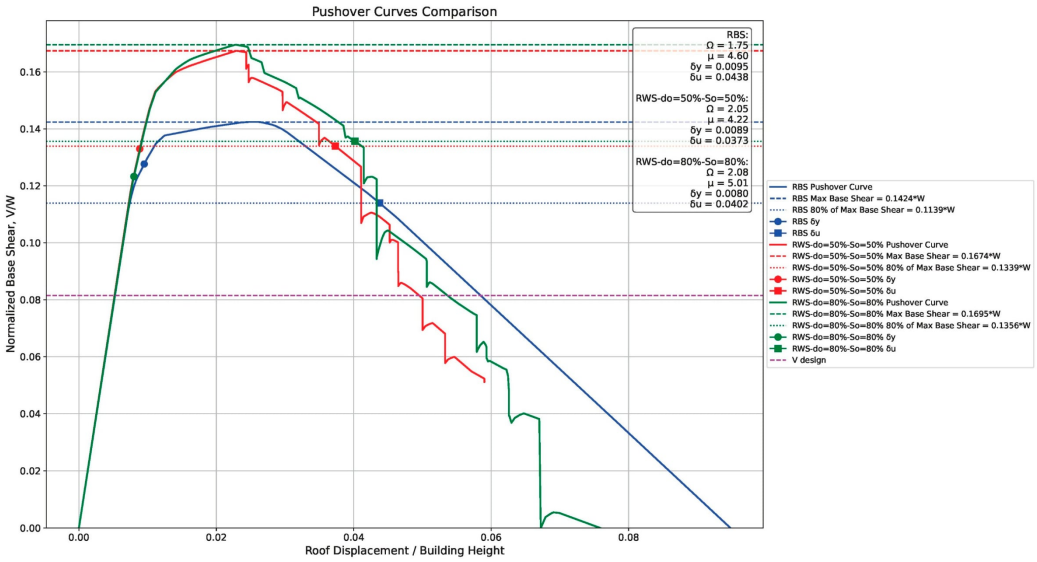


Figure 35. 4-storey frame pushover analysis curves.

4.2.3. 8-Storey Frame

RWS connections demonstrated higher peak strength and overstrength factors when compared to RBS connections, as shown in Figure 36. The post-peak behaviour of RWS connections showed more rapid strength degradation, but this is influenced by the imposed rotation limit. Despite earlier strength loss, RWS connections have maintained displacement ductility ratios (μ = 3.12 and 3.35) comparable to RBS (μ = 3.65).

4.2.4. 12-Storey Frame

RWS connections continued to show higher peak strength and overstrength factors, as shown in Figure 37. The difference in ductility between RWS and RBS configurations was less pronounced in taller structures. All connection types demonstrated adequate performance, with ductility ratios exceeding 2.0.

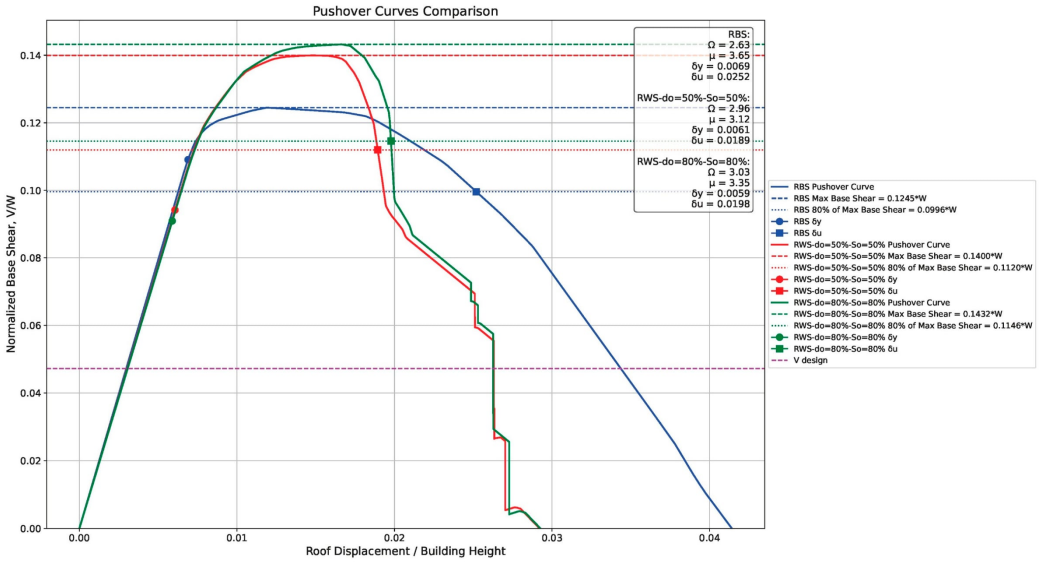


Figure 36. 8-storey frame pushover analysis curves.

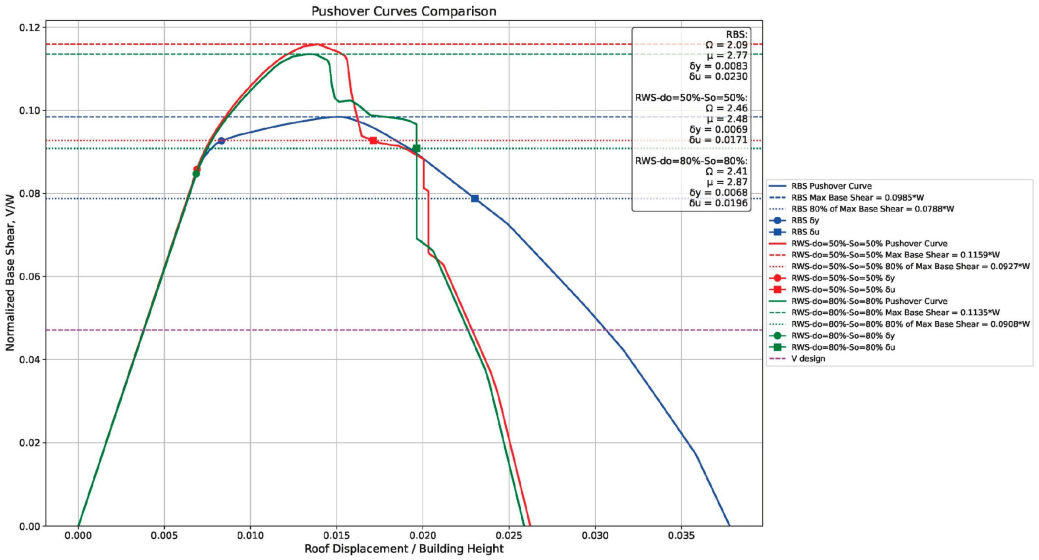


Figure 37. 12-storey frame pushover analysis curves.

4.2.5. 20-Storey Frame

In the case of the 20-storey frame, strength degradation initiated at an earlier stage in RWS connections compared to RBS connections, as illustrated in Figure 38. RWS connections with d_o = 80% and S_o = 80% showed the highest overstrength factor (Ω = 2.23), but lower ductility compared to the RBS connection. All connection types maintained acceptable performance levels, meeting code requirements.

It is important to note that the apparent earlier strength degradation in RWS connections is primarily due to the imposed ultimate rotation limit of approximately 0.05, while RBS connections are allowed to rotate up to 0.2. This limitation was set to control damage to the building, but it does not reflect an inherent lack of capacity in RWS connections [38]. In fact, all RWS connections demonstrated the ability to achieve interstorey drifts larger than 4%, thereby complying with performance targets set in ANSI/AISC 358-16, ANSI/AISC 341-16, and EC8 [43,60].

The results indicate that RWS connections, particularly the '80%–80%' (i.e., d_o = 80% and S_o = 80%) configuration often provides higher strength and comparable or superior ductility to RBS connections, especially in low to mid-rise structures. This suggests that

RWS connections could be a viable and potentially advantageous alternative to RBS connections in steel moment frames, offering enhanced structural performance while potentially simplifying fabrication and reducing costs [7,61].

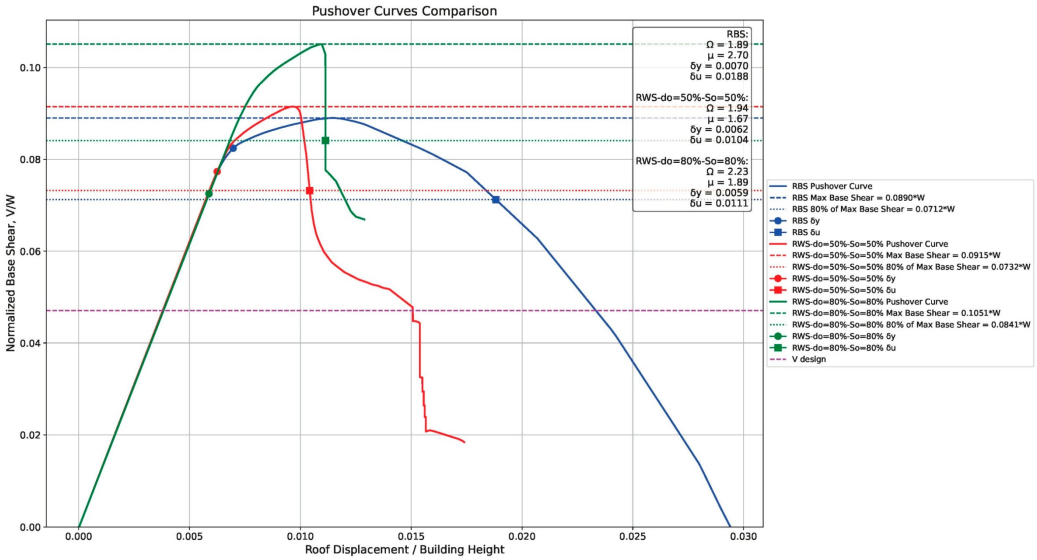


Figure 38. 20-storey frame pushover analysis curves.

5. Concluding Remarks

This paper significantly advances the understanding of Reduced Web Section (RWS) connections in steel moment frames through the application of machine learning (ML) and deep learning (DL) prediction modelling, followed by implementation in the design of several steel frames. The study analysed 154 specimens from experimental and finite element studies, focusing on non-composite welded and bolted end-plate connections, leading to a synthetic approach for defining the parameters of the modified Ibarra–Medina–Krawinkler (IMK) Bilin model, which is widely used in both industry and research. Multiple ML algorithms, including Random Forest, Neural Networks, Support Vector Regression, Gradient Boosting, XGBoost, and DL, were systematically evaluated using a robust cross-validation framework and comprehensive performance metrics. The research revealed complex interactions between web opening characteristics and structural behaviour, with web slenderness and span-to-depth ratios emerging as crucial parameters.

The findings demonstrate that RWS connections often provide higher strength and comparable or superior ductility to RBS connections, particularly in low- to mid-rise structures, with all RWS configurations achieving interstorey drifts exceeding 4%, meeting ANSI/AISC and EC8 performance targets. This research not only contributes valuable insights into RWS connection behaviour under seismic loading but also provides structural engineers with a practical tool for implementing these connections in performance-based seismic design.

The following detailed conclusions can be drawn:

- RWS connections demonstrate viable and often superior performance compared to traditional RBS connections in steel moment frames, particularly in low- to mid-rise structures.
- RWS connections consistently exhibit higher initial stiffness, peak strength, and over-strength factors compared to RBS connections across various frame heights (from 2 to 20 stories).
- The apparent earlier strength degradation in RWS connections is primarily due to the imposed ultimate rotation limit of 0.05 radians, which was set to control building

damage. Despite this limitation, RWS connections still achieve interstorey drifts larger than 4%, meeting performance targets set by ANSI/AISC and EC8 standards.

- ML and DL techniques, particularly XGBoost and Random Forest algorithms, demonstrate high accuracy in predicting modified Ibarra–Medina–Krawinkler (IMK) Bilin parameters for RWS connections, offering a powerful tool for efficient design and analysis.
- The study reveals complex interactions between web opening characteristics, beam length, and structural behaviour in RWS connections, providing valuable insights for optimising connection design.

Feature importance analysis highlights that different aspects of RWS connection behaviour are influenced by various geometric and material properties, with web slenderness and span-to-depth ratio consistently playing significant roles across multiple parameters.

- The developed predictive models offer a rapid and accurate method for estimating IMK Bilin parameters across a wide range of RWS connection configurations, potentially streamlining the design process for structural engineers.

Future research should focus on extending the database to include a wider range of geometric configurations and loading conditions, while priority should be given to experimental results. Also, the long-term performance and steel fatigue behaviour of RWS connections should be considered and included in the proposed models. Ultimately, the design guidelines for RWS connections based on the insights gained from this study should be further completed [49,62].

Author Contributions: A.K. conceptualization, methodology, formal analysis and investigation, data curation, software, validation, visualization, writing—original draft preparation, writing—review and editing. K.D.T. supervision, writing—review and editing. F.F.A. finite element data provision, writing—review and editing. A.A.-R. writing—review and editing. All authors have read and agreed to the published version of the manuscript.

Funding: This research received no external funding.

Data Availability Statement: The finite element data used in this study were provided by Fahad Falah Almutairi and Konstantinos Daniel Tsavdaridis. IMK Bilin Parameters Prediction for Non-Composite RWS Connection were generated using the online web tool: https://rws-predictor-132303566239.us-central1.run.app/ (accessed on 14 October 2026). Data supporting the findings of this study are available from the corresponding author upon reasonable request.

Conflicts of Interest: The authors declare no conflicts of interest.

Abbreviations

AI	Artificial Intelligence
AISC	American Institute of Steel Construction
ANSI	American National Standards Institute
AUC	Area Under the Curve
AUC-R	Area Under the Reliability Curve
BEEP-3-R	Bolted Extended End-Plate connection, 3-row
BEEP-4-R	Bolted Extended End-Plate connection, 4-row
DL	Deep Learning
EC8	Eurocode 8 (EN 1998: Design of structures for earthquake resistance)
EGF	Equivalent Gravity Frame
FE	Finite Element
GB	Gradient Boosting
GUI	Graphical User Interface
IMK	modified Ibarra–Medina–Krawinkler (model)

MAE	Mean Absolute Error
MAPE	Mean Absolute Percentage Error
ML	Machine Learning
MLP	Multi-Layer Perceptron
MRF	Moment-Resisting Frame
MSE	Mean Squared Error
NN	Neural Network
RBS	Reduced Beam Section
RF	Random Forest
RMSE	Root Mean Squared Error
ROC	Receiver Operating Characteristic
RWS	Reduced Web Section
SAC	SAC Joint Venture (SEAOC–ATC–CUREE partnership)
SVR	Support Vector Regression
XGBoost	Extreme Gradient Boosting

Nomenclature

h_b	Overall depth of the beam (mm)
t_w	Web thickness of the beam (mm)
b_f	Flange width of the beam (mm)
t_f	Flange thickness of the beam (mm)
L_b	Beam length (shear span) (mm)
d_o	Diameter of the web opening (mm)
S_o	Distance from the web-opening centreline to the column face (mm)
f_{yb}	Nominal yield strength of the beam steel (MPa)
h_b/t_w	Web slenderness (–)
$b_f/2t_f$	Flange slenderness (–)
L_b/h_b	Beam length (shear span) to depth ratio (–)
d_o/h_b	Opening diameter to beam depth ratio (–)
S_o/h_b	Opening position to beam depth ratio (–)
K_0	Elastic rotational stiffness (kN·m/rad)
a_s^+, a_s^-	Strain-hardening ratio (post-yield stiffness divided by elastic stiffness), positive/negative bending (–)
M_y^+, M_y^-	Effective yield moment, positive/negative bending (kN·m)
M_c, M_r	Capping (peak) moment and residual moment (kN·m)
Λ_S, Λ_C, Λ_A, Λ_K	Cyclic deterioration parameters for basic strength, post-capping strength, accelerated reloading stiffness and unloading stiffness deterioration (–)
c_S, c_C, c_A, c_K	Exponents defining the rate of the corresponding cyclic deterioration modes (–)
θ_p^+, θ_p^-	Pre-capping plastic rotation, positive/negative bending (rad)
θ_{pc}^+, θ_{pc}^-	Post-capping plastic rotation, positive/negative bending (rad)
θ_u^+, θ_u^-	Ultimate rotation capacity, positive/negative bending (rad)
κ^+, κ^-	Residual strength ratio, positive/negative bending (–)
D^+, D^-	Rate of cyclic deterioration in the positive/negative loading direction (–)
n	Elastic stiffness amplification factor of the Bilin material (–)
Ω	Overstrength factor (–)
μ	Displacement ductility ratio (–)

References

1. Mazzolani, F.M. *Steel Structures in Seismic Zones, in Seismic Resistant Steel Structures*; Mazzolani, F.M., Gioncu, V., Eds.; Springer: Weihburggasse, Vienna, 2000; pp. 1–17.
2. Astaneh-Asl, A. Post-earthquake stability of steel moment frames with damaged connections. *Connect. Steel Struct. III* **1996**, 391–402. [CrossRef]

3. Malley, J.O. Performance of moment resisting steel frames in the january 17, 1994 northridge earthquake. *Connect. Steel Struct. III* **1996**, 553–561. [CrossRef]
4. Sofias, C.E.; Pachoumis, D.T. Assessment of reduced beam section (RBS) moment connections subjected to cyclic loading. *J. Constr. Steel Res.* **2020**, *171*, 106151. [CrossRef]
5. Horton, T.A.; Hajirasouliha, I.; Davison, B.; Ozdemir, Z.; Abuzayed, I. Development of more accurate cyclic hysteretic models to represent RBS connections. *Eng. Struct.* **2021**, *245*, 112899. [CrossRef]
6. Naughton, D.T.; Tsavdaridis, K.D.; Maraveas, C.; Nicolaou, A. Pushover analysis of steel seismic resistant frames with reduced web section and reduced beam section connections. *Front. Built Environ.* **2017**, *3*, 59. [CrossRef]
7. Tsavdaridis, K.D.; Papadopoulos, T. A FE parametric study of RWS beam-to-column bolted connections with cellular beams. *J. Constr. Steel Res.* **2016**, *116*, 92–113. [CrossRef]
8. Valente, M.; Castiglioni, C.A.; Kanyilmaz, A. Dissipative devices for earthquake resistant composite steel structures: Bolted versus welded solution. *Bull. Earthq. Eng.* **2016**, *14*, 3613–3639. [CrossRef]
9. Valente, M.; Castiglioni, C.A.; Kanyilmaz, A. Numerical investigations of repairable dissipative bolted fuses for earthquake resistant composite steel frames. *Eng. Struct.* **2017**, *131*, 275–292, ISSN 0141-0296. [CrossRef]
10. Ibarra, L.F.; Krawinkler, H. Global Collapse of Frame Structures Under Seismic Excitations. 2005. Available online: https://stacks.stanford.edu/file/druid%3Adj885ym2486/TR152_Ibarra.pdf (accessed on 14 October 2026).
11. Tsavdaridis, K.D.; Faghih, F.; Nikitas, N. Assessment of perforated steel beam-to-column connections subjected to cyclic loading. *J. Earthq. Eng.* **2014**, *18*, 1302–1325. [CrossRef]
12. Zhang, X.; Zheng, S.; Zhao, X. Seismic performance of steel beam-to-column moment connections with different structural forms. *J. Constr. Steel Res.* **2019**, *158*, 130–142. [CrossRef]
13. Boushehri, K.; Tsavdaridis, K.D.; Cai, G. Seismic behaviour of RWS moment connections to deep columns with European sections. *J. Constr. Steel Res.* **2019**, *161*, 416–435. [CrossRef]
14. Nazaralizadeh, H.; Ronagh, H.; Memarzadeh, P.; Behnamfar, F. Cyclic performance of bolted end-plate RWS connection with vertical-slits. *J. Constr. Steel Res.* **2020**, *173*, 106236. [CrossRef]
15. Xu, Q.; Chen, H.; Li, W.; Zheng, S.; Zhang, X. Experimental investigation on seismic behavior of steel welded connections considering the influence of structural forms. *Eng. Fail. Anal.* **2022**, *139*, 106499. [CrossRef]
16. Horton, T. Predicting Reduced Beam Section (RBS) Connection Performance in Steel Moment Frames. Ph.D. Thesis, University of Sheffield, Sheffield, UK, 2021.
17. FEMA. FEMA 350—Recommended Seismic Design Criteria for New Steel Moment-Frame Buildings. Available online: https://www.seaoc.org (accessed on 14 October 2026).
18. Deng, C.G.; Bursi, O.S.; Zandonini, R. A hysteretic connection element and its applications. *Comput. Struct.* **2000**, *78*, 93–110. [CrossRef]
19. Patsialis, D.; Kyprioti, A.P.; Taflanidis, A.A. Bayesian calibration of hysteretic reduced order structural models for earthquake engineering applications. *Eng. Struct.* **2020**, *224*, 111204. [CrossRef]
20. Elkady, A.; Lignos, D.G. Effect of gravity framing on the overstrength and collapse capacity of steel frame buildings with perimeter special moment frames. *Earthq. Eng. Struct. Dyn.* **2015**, *44*, 1289–1307. [CrossRef]
21. Erfani, S.; Akrami, V.; Mohammad-nejad, A. Lateral load resisting behavior of steel moment frames with reduced web section (RWS) beams. *Structures* **2020**, *28*, 251–265. [CrossRef]
22. Roudsari, M.T.; Jamshidi K, H.; Zangeneh, M.M. Experimental and Numerical Investigation of IPE Reduced Beam Sections with Diagonal Web Stiffeners. *J. Earthq. Eng.* **2018**, *22*, 533–552. [CrossRef]
23. Aydin, E.; Ozturk, B.; Sahin, E. Investigation of behavior of adjacent planar steel frames connected with rigid bars under earthquake effects. In Proceedings of the 6th World Conference on Structural Control and Health Monitoring (6WCSCM), Barcelona, Spain, 15–17 July 2014.
24. Horton, T.A.; Hajirasouliha, I.; Davison, B.; Ozdemir, Z. Accurate prediction of cyclic hysteresis behaviour of RBS connections using Deep Learning Neural Networks. *Eng. Struct.* **2021**, *247*, 113156. [CrossRef]
25. Khoshkroodi, A.; Parvini Sani, H.; Aajami, M. Stacking Ensemble-Based Machine Learning Model for Predicting Deterioration Components of Steel W-Section Beams. *Buildings* **2024**, *14*, 240. [CrossRef]
26. Tasdemir, E.; Cetinkaya, M.Y.; Uysal, F.; El-Zahab, S. An Explainable Machine Learning-Based Prediction of Backbone Curves for Reduced Beam Section Connections Under Cyclic Loading. *Buildings* **2025**, *15*, 2307. [CrossRef]
27. Lignos, D.; Krawinkler, H. Sidesway Collapse of Deteriorating Structural Systems Under Seismic Excitations. 2012. Available online: https://stacks.stanford.edu/file/druid:yg701cw5473/TR%20177Lignos.pdf (accessed on 14 October 2026).
28. Almutairi, F.F.; Tsavdaridis, K.D. Capacity design assessment of composite reduced web section (RWS) connections. *Eng. Struct.* **2024**, *316*, 118558. [CrossRef]
29. Lignos, D.G.; Krawinkler, H. Deterioration modeling of steel components in support of collapse prediction of steel moment frames under earthquake loading. *J. Struct. Eng.* **2011**, *137*, 1291–1302. [CrossRef]

30. Bosco, M.; Marino, E.M.; Tirca, L.; Pollicino, A. Calibration of Ibarra-Krawinkler model for steel members with cold-formed hollow cross-section. *J. Constr. Steel Res.* **2024**, *217*, 108683. [CrossRef]
31. Bamshad, O.; Ghahremani Gargary, E. Development of modified Ibarra Krawinkler deterioration model for one-story steel plate shear wall. *Int. J. Steel Struct.* **2020**, *20*, 1574–1589. [CrossRef]
32. Qi, H.; Guo, W.; Zhang, Y. Monotonic and hysteretic model for H-shaped beams incorporating deterioration behavior owing to the local buckling. *Thin-Walled Struct.* **2020**, *157*, 107084. [CrossRef]
33. Şahin, B.; Macorini, L.; Izzuddin, B.A. Assessment of cyclic degradation effects in composite steel-concrete members. *J. Constr. Steel Res.* **2022**, *194*, 107308. [CrossRef]
34. Moammer, O.; Madsen, R.L.; Tort, C.; Hines, E.M. Predictive equations for shear link modeling toward collapse. *Eng. Struct.* **2017**, *151*, 599–612. [CrossRef]
35. Shayanfar, M.; Zaherbin, P.; Niaraki, P.J.; Eskandari, A. Force-displacement relation for lumped plasticity model of compact square concrete-filled steel tube columns. *Results Eng.* **2024**, *23*, 102619, ISSN 2590-1230. [CrossRef]
36. Chen, P.-Y.; Lee, K.-C.; Li, T.-L. Prediction of parameters in the Ibarra–Medina–Krawinkler model for reinforced concrete columns using random forest and active learning. *Soil Dyn. Earthq. Eng.* **2024**, *185*, 108902, ISSN 0267-7261. [CrossRef]
37. Zhou, X.; Li, J.; Yin, K. Numerical Simulation of Cyclic Degradations of Reinforced Concrete Columns: Model Parameter Calibration and Experimental Validation. *J. Earthq. Eng.* **2025**, *29*, 1356–1375. [CrossRef]
38. Almutairi, F.F.; Tsavdaridis, K.D.; Alonso-Rodriguez, A.; Hajirasouliha, I. Experimental investigation using demountable steel-concrete composite reduced web section (RWS) connections under cyclic loads. *Bull. Earthq. Eng.* **2024**, *22*, 1081–1110. [CrossRef]
39. Zhang, H.; Burton, H.; Sun, X. Rapid seismic damage state assessment of steel moment frames using machine learning. *Earthq. Eng. Struct. Dyn.* **2020**, *49*, 1070–1090.
40. Hwang, S.; Lignos, K.; Park, Y.J. Machine learning-based approaches for seismic demand estimation of steel moment-resisting frames. *Earthq. Spectra* **2021**, *37*, 1173–1201.
41. *ANSI/AISC 360-16*; Specification for Structural Steel Buildings. American Institute of Steel Construction (AISC): Chicago, IL, USA, 2016.
42. *EN 1993-1-1*; Eurocode 3: Design of Steel Structures—Part 1-1: General Rules and Rules for Buildings. European Committee for Standardization (CEN): Brussels, Belgium, 2005.
43. Prequalified Connections for Special and Intermediate Steel Moment Frames for Seismic Applications. 2016. Available online: https://www.aisc.org (accessed on 14 October 2026).
44. Luco, N.; Ellingwood, B.R.; Hamburger, R.O.; Hooper, J.D.; Kimball, J.K.; Kircher, C.A. Risk-targeted versus current seismic design maps for the conterminous United States. In *SEAOC 2007 Convention Proceedings*; Structural Engineers Association of California (SEAOC): Sacramento, CA, USA, 2007.
45. *ANSI/AISC 341-16*; Seismic Provisions for Structural Steel Buildings. American Institute of Steel Construction (AISC): Chicago, IL, USA, 2016.
46. Zorin, A.; Trofimov, A.; Abashev, D.; Exact, V.; Linderov, M.L. Using Machine Learning for Non-destructive Evaluation of Mechanical Properties of Steel Structures. *J. Mater. Eng. Perform.* **2026**, *35*, 15924–15932. [CrossRef]
47. Almutairi, F.F.; Tsavdaridis, K.D.; Alonso-Rodriguez, A. Hysteretic behaviour of composite reduced web section (RWS) connections for seismic applications. *J. Earthq. Eng.* **2023**, *28*, 1–36. [CrossRef]
48. Lignos, D.G.; Krawinkler, H.; Whittaker, A.S. Prediction and validation of sidesway collapse of two scale models of a 4-story steel moment frame. *Earthq. Eng. Struct. Dyn.* **2011**, *40*, 807–825. [CrossRef]
49. Darwin, D. *Steel Design Guide Series Steel and Composite Beams with Web Openings Design of Steel and Composite Beams with Web Openings*; American Institute of Steel Construction (AISC): Chicago, IL, USA, 2003.
50. Tsavdaridis, K.D.; D'Mello, C. Web buckling of perforated steel beams. *J. Constr. Steel Res.* **2011**, *67*, 1605–1620. [CrossRef]
51. Ibarra, L.F.; Medina, R.A.; Krawinkler, H. Hysteretic models that incorporate strength and stiffness deterioration. *Earthq. Eng. Struct. Dyn.* **2005**, *34*, 1489–1511. [CrossRef]
52. Krawinkler, H. Loading histories for cyclic tests in support of performance assessment of structural components. In Proceedings of the Proceedings, 3rd International Conference on Advances in Experimental Structural Engineering, San Francisco, CA, USA, 15–16 October 2009.
53. Chen, T.; Guestrin, C. XGBoost: A scalable tree boosting system. In *Proceedings of the 22nd ACM SIGKDD International Conference on Knowledge Discovery and Data Mining (KDD '16)*; ACM: New York, NY, USA, 2016; pp. 785–794. [CrossRef]
54. Wei, B.; Zheng, X.; Jiang, L.; Lai, Z.; Zhang, R.; Chen, J.; Yang, Z. Seismic response prediction and fragility assessment of high-speed railway bridges using machine learning technology. *Structures* **2024**, *66*, 106845. [CrossRef]
55. Truong, G.T.; Hwang, H.-J.; Kim, C.-S. Prediction of shear strength of RC deep beams using XGBoost regression with Bayesian optimization. *Eur. J. Environ. Civ. Eng.* **2023**, *27*, 4046–4066. [CrossRef]

56. Nguyen, H.D.; Dao, N.D.; Adeli, H. Prediction of seismic drift responses of planar steel moment frames using artificial neural network and extreme gradient boosting. *Eng. Struct.* **2021**, *242*, 112518. [CrossRef]
57. Saleem, N.; Mangalathu, S.; Ahmed, B.; Jeon, J.-S. Machine learning-based peak ground acceleration models for structural risk assessment using spatial data analysis. *Earthq. Eng. Struct. Dyn.* **2023**, *52*, 3815–3836. [CrossRef]
58. Taffese, W.Z.; Espinosa-Leal, L. Multitarget regression models for predicting compressive strength and chloride resistance of concrete. *J. Build. Eng.* **2023**, *72*, 106523. [CrossRef]
59. Elkady, A.; Lignos, D.G. Modeling of the composite action in fully restrained beam-to-column connections: Implications in the seismic design and collapse capacity of steel special moment frames. *Earthq. Eng. Struct. Dyn.* **2014**, *43*, 1935–1954. [CrossRef]
60. *EN 1998-1*; Eurocode 8: Design of Structures for Earthquake Resistance—Part 1: General Rules, Seismic Actions and Rules for Buildings. European Committee for Standardization: Brussels, Belgium, 2004.
61. A, S.M.; Daniel, T.K.; Satoshi, Y. Comprehensive FE Study of the Hysteretic Behavior of Steel–Concrete Composite and Noncomposite RWS Beam-to-Column Connections. *J. Struct. Eng.* **2018**, *144*, 04018150. [CrossRef]
62. Fares, S.S.; Eng, P.; Coulson, J.; Dinehart, D.W. *Castellated and Cellular Beam Design 31 Steel Design Guide*; American Institute of Steel Construction (AISC): Chicago, IL, USA, 2016.

Disclaimer/Publisher's Note: The statements, opinions and data contained in all publications are solely those of the individual author(s) and contributor(s) and not of MDPI and/or the editor(s). MDPI and/or the editor(s) disclaim responsibility for any injury to people or property resulting from any ideas, methods, instructions or products referred to in the content.